

Probing a Fifth Force in Muonic Atoms through Lamb Shifts and Hyperfine Structure

Xiaoxuan Lin^{1,2,*}, Qian Wu^{3,2,4,†}, Wei Kou^{5,2,5,6,7,‡} and Xurong Chen^{2,5,6,7,§}

¹*College of Physics Science and Technology, Hebei University, Baoding 071002, China*

²*Institute of Modern Physics, Chinese Academy of Sciences, Lanzhou 730000, China*

³*School of Physics, Nanjing University, Nanjing, Jiangsu 210093, China*

⁴*Nuclear Many-Body Theory Laboratory, RIKEN Nishina Center, RIKEN, Wako 351-0198, Japan*

⁵*School of Nuclear Science and Technology, University of Chinese Academy of Sciences, Beijing 100049, China*

⁶*Southern Center for Nuclear Science Theory (SCNT), Institute of Modern Physics, Chinese Academy of Sciences, Huizhou 516000, Guangdong Province, China*

⁷*State Key Laboratory of Heavy Ion Science and Technology, Institute of Modern Physics, Chinese Academy of Sciences, Lanzhou 730000, China*

Motivated by the ATOMKI anomalies observed in ^8Be and ^4He transitions, we present a systematic survey of $X17$ -induced Lamb shifts and hyperfine splittings in muonic atoms with stable nuclei up to $Z \leq 15$. The muon–nucleus bound-state problem is solved within the Gaussian Expansion Method using a unified Hamiltonian that includes the standard electromagnetic baseline together with vector- and pseudoscalar- $X17$ exchange. A central feature of this work is that the Lamb-shift and hyperfine sectors are treated with different nuclear couplings: the spin-independent Lamb shift is described by a coherent vector muon–nucleus interaction, while the spin-dependent hyperfine sector is constructed isotope by isotope from shell-model spin fractions. Benchmark muon couplings are chosen in accordance with the 2025 Muon $g-2$ result. We find a clear complementarity between mediator hypotheses. The vector Lamb-shift signal grows strongly toward heavier nuclei, while in the hyperfine sector the vector scenario preferentially enhances odd- N nuclei and the pseudoscalar scenario favors odd- Z systems. To compare different systems on a common experimental footing, we introduce the signal-to-precision ratio. Among systems with existing precision benchmarks, the most promising near-term probes of the vector Lamb-shift channel are μd , $\mu^3\text{He}^+$, and $\mu^4\text{He}^+$. For future spectroscopy, the largest absolute vector Lamb-shift signal is predicted in $\mu^{31}\text{P}$, while the leading $1S_{1/2}$ hyperfine targets are $\mu^{29}\text{Si}$ for the vector scenario and $\mu^{31}\text{P}$ for the pseudoscalar scenario. The dominant theoretical uncertainty arises from the Schmidt-model treatment of nuclear spin content, indicating that beyond-Schmidt nuclear-structure input will be the key ingredient for quantitative follow-up studies of the leading hyperfine targets.

I. INTRODUCTION

The anomalous internal pair creation reported by the ATOMKI collaboration in excited transitions of ^8Be [1] and ^4He [2] has motivated sustained interest in a light boson with a mass near 17 MeV. If such a particle exists, it would signal a new force beyond the Standard Model and would have broad implications for light-mediator phenomenology and precision tests of fundamental interactions. Among the proposed explanations, the protophobic vector scenario remains one of the most widely discussed possibilities [3], while pseudoscalar and axial-vector alternatives have also been explored extensively [4, 5]. A key question is how to construct observables that are sensitive not only to the existence of such a mediator, but also to its coupling pattern and spin-parity structure.

Muonic atoms provide a particularly favorable setting for such tests. Because the muon is about 200 times heavier than the electron, its Bohr orbit is compressed to the nuclear scale, greatly enhancing sensitivity to short-range Yukawa-type interactions relative to ordinary atoms. The success of high-precision muonic spectroscopy in the proton-radius puzzle demonstrated that tiny level shifts in muonic systems can be measured with remarkable accuracy [6], while more recent measurements in the helium sector have shown that sub-meV sensitivity is achievable in practice [7]. For a mediator with $m_X \simeq 16.7$ MeV, the corresponding range $m_X^{-1} \approx 12$ fm overlaps closely with the region most strongly probed by low-lying muonic wave functions in light and medium-light nuclei. Muonic atoms are therefore natural laboratories for searching for short-range MeV-scale forces.

Most previous discussions of possible $X17$ effects in muonic atoms have focused on only a few light systems, especially muonic hydrogen and deuterium [8–10]. While such systems are theoretically clean and experimentally important, they do not by themselves reveal the broader nuclear systematics expected from a new short-range interaction. In

* x-x.lin@stumail.hbu.edu.cn

† qwu@nju.edu.cn

‡ kouwei@impcas.ac.cn

§ xchen@impcas.ac.cn (Corresponding Author)



FIG. 1. Schematic illustration of muon–nucleon interactions mediated by a light boson X_{17} . Panel (a) shows vector exchange, which contributes to both the Lamb shift and hyperfine structure. Panel (b) shows pseudoscalar exchange, which contributes only to the hyperfine sector at leading order.

particular, different observables probe different combinations of hadronic couplings. For a vector mediator, the spin-independent $2S_{1/2}$ – $2P_{1/2}$ Lamb shift is governed by a coherent muon–nucleus interaction and therefore depends on the total nuclear vector charge summed over all nucleons. Hyperfine splittings, by contrast, are spin dependent and probe the proton and neutron spin content of each nucleus. The optimal targets for Lamb-shift and hyperfine measurements therefore need not coincide, and a meaningful survey must treat the two sectors differently at the nuclear level.

In this work, we present a unified study of X_{17} -induced Lamb shifts and hyperfine splittings in muonic atoms with stable nuclei up to $Z \leq 15$. Our analysis makes three main advances. First, we perform a nucleus-by-nucleus survey across the light and medium-light region rather than restricting attention to a few benchmark systems. Second, we construct the two observables with different nuclear inputs: the vector Lamb shift is described through the coherent muon–nucleus coupling proportional to $Zh'_p + Nh'_n$, whereas the hyperfine sector is built isotope by isotope from proton and neutron spin fractions. Third, we connect the predicted signals directly to experimental reach by introducing the signal-to-precision ratio

$$\mathcal{R} \equiv |\Delta E_{X_{17}}|/\delta E,$$

where δE denotes the achieved or projected precision for the relevant transition. This quantity provides a simple way to compare systems with very different absolute energy scales on common experimental footing.

Several robust patterns emerge from the present study. The vector Lamb-shift channel is coherently enhanced and grows strongly toward heavier nuclei. In the hyperfine sector, the vector and pseudoscalar hypotheses exhibit complementary target selectivity because they weight neutron and proton spin content differently: vector exchange preferentially enhances odd- N nuclei, whereas pseudoscalar exchange favors odd- Z systems. This observable-dependent separation makes comparative muonic spectroscopy a promising tool not only for constraining a possible fifth force, but also for discriminating among mediator hypotheses if a signal is observed.

Our calculations are performed within the Gaussian Expansion Method [11], using a unified Hamiltonian that includes the standard electromagnetic baseline together with vector- and pseudoscalar- X_{17} exchange. Nuclear masses, charge radii, magnetic moments, and related inputs are taken from evaluated databases [12–14], while the nuclear spin structure is treated at the independent-particle shell-model (Schmidt-model) level [15, 16]. On the leptonic side, we adopt benchmark muon couplings guided by the updated Muon $g-2$ situation. Benchmark comparisons with published results for light muonic atoms show that the electromagnetic baseline is sufficient for target identification, while the dominant theoretical uncertainty in the hyperfine sector arises from the Schmidt-model treatment of nuclear spin fractions rather than from the atomic calculation itself.

The remainder of this paper is organized as follows. Section II presents the theoretical framework, including the Hamiltonian, coupling choices, nuclear spin input, and validation of the numerical implementation. Section III gives the predicted Lamb-shift and hyperfine signals for both mediator hypotheses and discusses their implications for experimental target selection. Section IV summarizes the main conclusions and outlines the prospects for ongoing and future muonic-atom spectroscopy programs. Comprehensive numerical results are collected in Appendices B–D.

II. THEORETICAL FRAMEWORK

A. The System Hamiltonian

We treat the problem as a muon–nucleus two-body system with Hamiltonian

$$H = H_0 + H_{\text{fs}} + H_F + H^{X_{17}}. \quad (1)$$

The atomic calculation is formulated entirely in terms of the relative coordinate between the muon and the center-of-mass of the nucleus. The underlying new-physics interaction is defined at the muon–nucleon level and then mapped onto muon–nucleon operators through two distinct procedures, depending on the observable. For the hyperfine sector, the spin-dependent muon–nucleon interaction is mapped via the nuclear spin fractions $\Delta_{p,n}$ introduced in Sec. **IID**, yielding spin-fraction-weighted effective couplings. For the spin-independent vector Lamb shift, the nucleon-level couplings are instead summed coherently over all Z protons and N neutrons, as described below and in Sec. **IIIB**. This two-step procedure ensures that the nuclear-structure information appropriate to each observable is cleanly separated from the atomic-physics calculation.

The leading Schrödinger Hamiltonian contains the kinetic energy with reduced mass and the point Coulomb potential,

$$H_0 = \frac{\mathbf{p}^2}{2m_r} - \frac{Z\alpha}{r}, \quad m_r \equiv \frac{m_\mu m_N}{m_\mu + m_N}. \quad (2)$$

Following the standard Breit–Pauli expansion used in muonic atoms, the relativistic, Darwin/finite-size, and leptonic spin–orbit contributions are organized as Ref. [9]

$$H_{\text{fs}} = -\frac{\mathbf{p}^4}{8m_\mu^3} - \frac{\mathbf{p}^4}{8m_N^3} + \frac{\pi Z\alpha}{2} \left(\frac{4\langle r_N^2 \rangle}{3} + \frac{1}{m_\mu^2} + \frac{1}{m_N^2} \right) \delta^3(\mathbf{r}) \\ + \frac{Z\alpha}{4m_\mu^2 r^3} \left(1 + \frac{2m_\mu}{m_N} \right) \mathbf{L} \cdot \boldsymbol{\sigma}_\mu + V_{\text{Ueh}}(r), \quad (3)$$

where $\langle r_N^2 \rangle$ is the mean-square nuclear charge radius.

In the present work, the Uehling vacuum-polarization potential enters only as a background QED effect: its role is to provide the correct order of magnitude for the standard Lamb-shift contribution against which we compare the much smaller $X17$ -induced shifts. Since our primary focus is on the new-physics correction from $X17$, and not on a high-precision re-evaluation of the vacuum-polarization effect itself, it is sufficient for our purposes to employ a simple point-nucleus model for the Uehling potential.

The Uehling vacuum-polarization potential was first derived in Ref. [17] in the form

$$V_{\text{Ueh}}(r) = -\frac{Z\alpha}{r} \frac{\alpha}{\pi} \int_0^1 (1-u^2) du \int_1^\infty \exp\left[-\frac{2rz}{\lambda_0 \sqrt{1-u^2}}\right] \frac{dz}{z}, \quad (4)$$

where $\lambda_0 = \hbar/(m_e c)$ is the Compton wavelength of the electron.

The Fermi Hamiltonian H_F (see Eq. (10) of Ref. [18]) reads

$$H_F = \frac{g_N \alpha}{m_\mu m_N} \left[\frac{\pi}{3} \boldsymbol{\sigma}_\mu \cdot \boldsymbol{\sigma}_N \delta^{(3)}(\mathbf{r}) + \frac{3(\boldsymbol{\sigma}_\mu \cdot \mathbf{r})(\boldsymbol{\sigma}_N \cdot \mathbf{r}) - r^2 \boldsymbol{\sigma}_\mu \cdot \boldsymbol{\sigma}_N}{8r^5} + \frac{\boldsymbol{\sigma}_N \cdot \mathbf{L}}{4r^3} \right]. \quad (5)$$

For a vector $X17$, the 00 component of the propagator generates a leading, spin-independent Yukawa interaction. At the muon–nucleon level, coherently summing over all Z protons and N neutrons yields

$$V_X(r) = \frac{h'_\mu}{4\pi} (Zh'_p + Nh'_n) \frac{e^{-m_X r}}{r}, \quad (6)$$

which governs the $2S_{1/2}$ – $2P_{1/2}$ Lamb shift discussed in Sec. **IIIB**. Because Eq. (6) sums the vector charge over the entire nuclear bulk, it is distinct from the spin-fraction-weighted prescription used in the hyperfine sector (Sec. **IID**), which retains only the spin-carrying valence nucleon(s). The induced hyperfine Hamiltonian (vector exchange) is

$$H_{\text{HFS,V}} = \frac{h'_\mu h_N'^{(\text{eff})}}{16\pi m_\mu m_N} \left[-\frac{8\pi}{3} \delta^{(3)}(\mathbf{r}) \boldsymbol{\sigma}_\mu \cdot \boldsymbol{\sigma}_N - m_X^2 \frac{\boldsymbol{\sigma}_\mu \cdot \mathbf{r} \boldsymbol{\sigma}_N \cdot \mathbf{r} - r^2 \boldsymbol{\sigma}_\mu \cdot \boldsymbol{\sigma}_N}{r^3} e^{-m_X r} \right. \\ \left. - (1 + m_X r) \frac{3\boldsymbol{\sigma}_\mu \cdot \mathbf{r} \boldsymbol{\sigma}_N \cdot \mathbf{r} - r^2 \boldsymbol{\sigma}_\mu \cdot \boldsymbol{\sigma}_N}{r^5} e^{-m_X r} - \left(2 + \frac{m_\mu}{m_N} \right) \frac{(1 + m_X r)}{r^3} \boldsymbol{\sigma}_N \cdot \mathbf{L} e^{-m_X r} \right], \quad (7)$$

where $h_N'^{(\text{eff})} = h'_p \Delta_p + h'_n \Delta_n$ is the spin-fraction-weighted effective coupling defined in Eq. (51).

For a pseudoscalar $X17$ with pointlike $i\gamma_5$ couplings, the tree-level exchange induces a purely spin-dependent potential. Because its matrix elements vanish in the spin-averaged centroids of the nS and nP levels, this potential does

not generate an independent shift of the level centroids comparable to the vector Lamb shift; rather, it redistributes the energy within each hyperfine multiplet and thereby modifies the observable hyperfine splittings. The corresponding hyperfine Hamiltonian is

$$H_{\text{HFS},A} = \frac{h_\mu h_N^{(\text{eff})}}{16\pi m_\mu m_N} \left[\frac{4\pi}{3} \delta^{(3)}(\mathbf{r}) \boldsymbol{\sigma}_\mu \cdot \boldsymbol{\sigma}_N - m_X^2 \frac{(\boldsymbol{\sigma}_\mu \cdot \mathbf{r})(\boldsymbol{\sigma}_N \cdot \mathbf{r})}{r^3} e^{-m_X r} + (1 + m_X r) \frac{3(\boldsymbol{\sigma}_\mu \cdot \mathbf{r})(\boldsymbol{\sigma}_N \cdot \mathbf{r}) - r^2 \boldsymbol{\sigma}_\mu \cdot \boldsymbol{\sigma}_N}{r^5} e^{-m_X r} \right], \quad (8)$$

where $h_N^{(\text{eff})} = h_p \Delta_p + h_n \Delta_n$.

On spherically symmetric S -state wave functions one may use the angular averages

$$(\boldsymbol{\sigma}_\mu \cdot \mathbf{r})(\boldsymbol{\sigma}_N \cdot \mathbf{r}) \longrightarrow \frac{1}{3} r^2 \boldsymbol{\sigma}_\mu \cdot \boldsymbol{\sigma}_N, \quad \boldsymbol{\sigma}_N \cdot \mathbf{L} \longrightarrow 0, \quad (9)$$

so that

$$H_{\text{HFS},V} \rightarrow -\frac{h'_\mu h_N^{(\text{eff})}}{24\pi m_\mu m_N} \boldsymbol{\sigma}_\mu \cdot \boldsymbol{\sigma}_N \left[4\pi \delta^{(3)}(\mathbf{r}) - \frac{m_X^2}{r} e^{-m_X r} \right]. \quad (10)$$

$$H_{\text{HFS},A} \rightarrow \frac{h_\mu h_N^{(\text{eff})}}{48\pi m_\mu m_N} \boldsymbol{\sigma}_\mu \cdot \boldsymbol{\sigma}_N \left[4\pi \delta^{(3)}(\mathbf{r}) - \frac{m_X^2}{r} e^{-m_X r} \right]. \quad (11)$$

$$H_F \rightarrow \frac{g_N \alpha}{m_\mu m_N} \frac{\pi}{3} \boldsymbol{\sigma}_\mu \cdot \boldsymbol{\sigma}_N \delta^{(3)}(\mathbf{r}). \quad (12)$$

For P states it is convenient to separate angles and radius via $\mathbf{r} = r \hat{\mathbf{r}}$:

$$(\boldsymbol{\sigma}_\mu \cdot \mathbf{r})(\boldsymbol{\sigma}_N \cdot \mathbf{r}) = r^2 (\boldsymbol{\sigma}_\mu \cdot \hat{\mathbf{r}})(\boldsymbol{\sigma}_N \cdot \hat{\mathbf{r}}) = \frac{r^2}{3} [\boldsymbol{\sigma}_\mu \cdot \boldsymbol{\sigma}_N + S_{12}], \quad S_{12} = 3(\boldsymbol{\sigma}_\mu \cdot \hat{\mathbf{r}})(\boldsymbol{\sigma}_N \cdot \hat{\mathbf{r}}) - \boldsymbol{\sigma}_\mu \cdot \boldsymbol{\sigma}_N. \quad (13)$$

Matrix elements are evaluated in the coupled basis $|((L s_\mu) J S_N) F m_F\rangle$. Projectors onto fixed J satisfy

$$\mathbb{P}_J \mathbf{L} \mathbb{P}_J = \alpha_J \mathbf{J}, \quad \mathbb{P}_J \boldsymbol{\sigma}_\mu \mathbb{P}_J = 2(1 - \alpha_J) \mathbf{J}, \quad \alpha_J = \frac{J(J+1) + L(L+1) - s_\mu(s_\mu+1)}{2J(J+1)}. \quad (14)$$

With $\boldsymbol{\sigma}_N \equiv 2\mathbf{S}_N$ and

$$\Delta \equiv F(F+1) - J(J+1) - S_N(S_N+1), \quad \mathbf{J} \cdot \boldsymbol{\sigma}_N = \Delta, \quad (15)$$

the F -resolved expectation values take the universal form (at fixed L, s_μ, J):

$$\langle \mathbf{L} \cdot \boldsymbol{\sigma}_N \rangle = \alpha_J \Delta, \quad \langle \boldsymbol{\sigma}_\mu \cdot \boldsymbol{\sigma}_N \rangle = 2(1 - \alpha_J) \Delta, \quad \langle \mathbf{L} \cdot \boldsymbol{\sigma}_\mu \rangle = J(J+1) - L(L+1) - s_\mu(s_\mu+1). \quad (16)$$

For $1S_{1/2}$ one has $L = 0, J = \frac{1}{2}$, hence $\alpha_{1/2} = 0$ and

$$\langle \mathbf{L} \cdot \boldsymbol{\sigma}_\mu \rangle = 0, \quad \langle \mathbf{L} \cdot \boldsymbol{\sigma}_N \rangle = 0, \quad \langle \boldsymbol{\sigma}_\mu \cdot \boldsymbol{\sigma}_N \rangle = 2\Delta.$$

For $2P_{1/2}$ ($L = 1, s_\mu = \frac{1}{2}, J = \frac{1}{2}$) one finds $\alpha_{1/2} = 4/3$, thus

$$\langle \mathbf{L} \cdot \boldsymbol{\sigma}_N \rangle = \frac{4}{3}\Delta, \quad \langle \boldsymbol{\sigma}_\mu \cdot \boldsymbol{\sigma}_N \rangle = -\frac{2}{3}\Delta.$$

Treating S_{12} as a scalar coupling of rank-2 tensors yields, for $2P_{1/2}$,

$$\langle (\boldsymbol{\sigma}_\mu \cdot \hat{\mathbf{r}})(\boldsymbol{\sigma}_N \cdot \hat{\mathbf{r}}) \rangle = -\frac{14}{27}\Delta, \quad \langle S_{12} \rangle = -\frac{8}{9}\Delta. \quad (17)$$

These obey the exact identity

$$\frac{1}{8} \langle S_{12} \rangle + \frac{1}{4} \langle \boldsymbol{\sigma}_N \cdot \mathbf{L} \rangle = -\frac{1}{3} \langle \boldsymbol{\sigma}_\mu \cdot \boldsymbol{\sigma}_N \rangle, \quad (18)$$

TABLE III. $\langle \mathbf{L} \cdot \boldsymbol{\sigma}_N \rangle$ and $\langle \boldsymbol{\sigma}_\mu \cdot \boldsymbol{\sigma}_N \rangle$ for $2P_{1/2}$ (Pauli normalization).

S_N	$\langle \mathbf{L} \cdot \boldsymbol{\sigma}_N \rangle$		$\langle \boldsymbol{\sigma}_\mu \cdot \boldsymbol{\sigma}_N \rangle$	
	$F = S_N - \frac{1}{2}$	$F = S_N + \frac{1}{2}$	$F = S_N - \frac{1}{2}$	$F = S_N + \frac{1}{2}$
$\frac{1}{2}$	-2	$+\frac{2}{3}$	+1	$-\frac{1}{3}$
1	$-\frac{8}{3}$	$+\frac{4}{3}$	$+\frac{4}{3}$	$-\frac{2}{3}$
$\frac{3}{2}$	$-\frac{10}{3}$	+2	$+\frac{5}{3}$	-1
$\frac{5}{2}$	$-\frac{14}{3}$	$+\frac{10}{3}$	$+\frac{7}{3}$	$-\frac{5}{3}$

TABLE IV. $\langle (\boldsymbol{\sigma}_\mu \cdot \mathbf{r})(\boldsymbol{\sigma}_N \cdot \mathbf{r}) \rangle$ for $2P_{1/2}$ (Pauli normalization; angle-radius separated). We first evaluate the pure angular factor $\langle (\boldsymbol{\sigma}_\mu \cdot \hat{\mathbf{r}})(\boldsymbol{\sigma}_N \cdot \hat{\mathbf{r}}) \rangle = -\frac{14}{27} \Delta$ with $\Delta = F(F+1) - J(J+1) - S_N(S_N+1)$, $J = \frac{1}{2}$, and then multiply by r^2 .

S_N	$\langle (\boldsymbol{\sigma}_\mu \cdot \mathbf{r})(\boldsymbol{\sigma}_N \cdot \mathbf{r}) \rangle$	
	$F = S_N - \frac{1}{2}$	$F = S_N + \frac{1}{2}$
$\frac{1}{2}$	$\frac{7}{9} r^2$	$-\frac{7}{27} r^2$
1	$\frac{28}{27} r^2$	$-\frac{14}{27} r^2$
$\frac{3}{2}$	$\frac{35}{27} r^2$	$-\frac{7}{9} r^2$
$\frac{5}{2}$	$\frac{49}{27} r^2$	$-\frac{35}{27} r^2$

which is a convenient diagnostic for implementations. For S waves, the tensor reduces to $(\boldsymbol{\sigma}_\mu \cdot \mathbf{r})(\boldsymbol{\sigma}_N \cdot \mathbf{r}) \rightarrow \frac{r^2}{3} \boldsymbol{\sigma}_\mu \cdot \boldsymbol{\sigma}_N$, and the spin-orbit terms vanish.

TABLE I. $\langle \mathbf{L} \cdot \boldsymbol{\sigma}_\mu \rangle$ for $1S_{1/2}$ and $2P_{1/2}$. Here $\boldsymbol{\sigma}_\mu$ is the muon spin operator (Pauli convention).

State	$\langle \mathbf{L} \cdot \boldsymbol{\sigma}_\mu \rangle$
$1S_{1/2}$	0
$2P_{1/2}$	-2

TABLE II. $\langle \mathbf{L} \cdot \boldsymbol{\sigma}_N \rangle$ and $\langle \boldsymbol{\sigma}_\mu \cdot \boldsymbol{\sigma}_N \rangle$ for $1S_{1/2}$ (Pauli normalization).

S_N	$\langle \mathbf{L} \cdot \boldsymbol{\sigma}_N \rangle$	$\langle \boldsymbol{\sigma}_\mu \cdot \boldsymbol{\sigma}_N \rangle$	
		$F = S_N - \frac{1}{2}$	$F = S_N + \frac{1}{2}$
$\frac{1}{2}$	0	-3	+1
1	0	-4	+2
$\frac{3}{2}$	0	-5	+3
$\frac{5}{2}$	0	-7	+5

B. GEM implementation

We start from the Rayleigh–Ritz principle on the Hilbert space \mathcal{H} of square-integrable two-body wavefunctions. The stationary states minimize the energy functional under the unit-norm constraint,

$$\mathcal{F}[\psi, \lambda] = \langle \psi | \hat{H} | \psi \rangle - \lambda (\langle \psi | \psi \rangle - 1), \quad \delta \mathcal{F} = 0, \quad (19)$$

which yields the Euler–Lagrange condition $(\hat{H} - \lambda)|\psi\rangle = 0$ with $\lambda = E$.

For a central field it is natural to separate angles and solve, for each partial wave (L, m) ,

$$\left[-\frac{\nabla^2}{2\mu} + V(r) \right] \psi_{Lm}(\mathbf{r}) = E \psi_{Lm}(\mathbf{r}), \quad \mu = \frac{m_\mu m_N}{m_\mu + m_N}. \quad (20)$$

To make the constrained minimization explicit, expand $|\psi\rangle = \sum_j c_j |\phi_j\rangle$ in an arbitrary (generally non-orthogonal) set $\{|\phi_j\rangle\} \subset \mathcal{H}$. In coefficient space the functional becomes the Rayleigh quotient

$$\mathcal{F}(\mathbf{c}, \lambda) = \mathbf{c}^\dagger H \mathbf{c} - \lambda(\mathbf{c}^\dagger N \mathbf{c} - 1), \quad H_{ij} = \langle \phi_i | \hat{H} | \phi_j \rangle, \quad N_{ij} = \langle \phi_i | \phi_j \rangle, \quad (21)$$

and stationarity with respect to \mathbf{c}^* gives the generalized Hermitian eigenproblem

$$H \mathbf{c} = E N \mathbf{c}. \quad (22)$$

Since N is positive-definite on the span of $\{|\phi_j\rangle\}$, (22) can be reduced to a standard Hermitian problem $B^{-1} H B^{-1} \mathbf{y} = E \mathbf{y}$ with the variational upper-bound property and monotone convergence as the span is enlarged.

Within the Gaussian Expansion Method (GEM) [11, 19, 20], we choose a radial basis that retains analytic integrability while densely sampling short and long distances:

$$\psi_{\ell m}(\mathbf{r}) = \sum_{n=1}^{n_{\max}} c_{n\ell} \phi_{n\ell m}^G(\mathbf{r}), \quad (23)$$

$$\phi_{n\ell m}^G(\mathbf{r}) = \mathcal{N}_{n\ell} r^\ell e^{-\nu_n r^2} Y_{\ell m}(\hat{\mathbf{r}}), \quad \mathcal{N}_{n\ell} = \left[\frac{2^{\ell+2} (2\nu_n)^{\ell+\frac{3}{2}}}{\sqrt{\pi} (2\ell+1)!!} \right]^{1/2}, \quad (24)$$

$$N_{n,n'} = \langle \phi_{n\ell m}^G | \phi_{n'\ell m}^G \rangle = \left(\frac{2\sqrt{\nu_n \nu_{n'}}}{\nu_n + \nu_{n'}} \right)^{\ell+\frac{3}{2}}. \quad (25)$$

with geometric placement of ranges to ensure near-uniform resolution in $\log r$,

$$\nu_n = \frac{1}{r_n^2}, \quad r_n = r_{\min} a^{n-1}, \quad a = \left(\frac{r_{\max}}{r_{\min}} \right)^{1/(n_{\max}-1)}, \quad n = 1, \dots, n_{\max}. \quad (26)$$

Plugging (23) into (20) and using (21) we obtain, for each L ,

$$\sum_{n'=1}^{n_{\max}} \left[T_{nn'}^{(L)} + V_{nn'}^{(L)} - E N_{nn'}^{(L)} \right] c_{n'L} = 0. \quad (27)$$

C. Couplings to X17

On the hadronic side we adopt two convenient benchmarks. First, for a *vector* mediator we write

$$h'_p = \epsilon_p e, \quad h'_n = \epsilon_n e, \quad (28)$$

with nucleon charges built from quark charges,

$$\epsilon_p = 2\epsilon_u + \epsilon_d, \quad \epsilon_n = \epsilon_u + 2\epsilon_d. \quad (29)$$

Motivated by fits to the ^8Be anomaly we take the working values

$$\epsilon_p = 8 \times 10^{-4}, \quad \epsilon_n = \frac{1}{100}, \quad (30)$$

which imply

$$h'_p = \epsilon_p e \simeq 2.42 \times 10^{-4}, \quad (31)$$

$$h'_n = \epsilon_n e \simeq 3.03 \times 10^{-3}, \quad (32)$$

with ϵ_n controlled by $\epsilon_{u,d}$ as above [3].

Second, for a pseudoscalar mediator we take couplings proportional to fermion masses,

$$h_p = \xi_p \frac{m_p}{v}, \quad h_n = \xi_n \frac{m_n}{v}, \quad v = 246 \text{ GeV}, \quad (33)$$

which, using standard nucleon matrix elements (as in [8]), give

$$h_p \simeq \frac{m_p}{v} (-0.40 \xi_u - 1.71 \xi_d) \approx -2.4 \times 10^{-3}, \quad (34)$$

$$h_n \simeq \frac{m_n}{v} (-0.40 \xi_u + 0.85 \xi_d) \approx 5.1 \times 10^{-4}. \quad (35)$$

Turning to the lepton side, we consider both a vector and a pseudoscalar $X17$ that couple to the muon. For the vector hypothesis we write

$$\mathcal{L}_{X,V} = -h'_\mu \bar{\mu} \gamma^\nu \mu X_\nu \quad (36)$$

and for the pseudoscalar hypothesis

$$\mathcal{L}_{X,A} = -h_\mu \bar{\mu} i \gamma_5 \mu A. \quad (37)$$

At one loop these interactions shift the muon anomaly $a_\mu = (g-2)_\mu/2$. For a mediator around $m_X \simeq 16.7$ MeV, the standard one-loop expressions read [21, 22]

$$\Delta a_\mu^{(V)} = \frac{(h'_\mu)^2}{8\pi^2} \frac{m_\mu^2}{m_X^2} \int_0^1 dx \frac{x^2(2-x)}{(1-x)\left(1 - \frac{m_\mu^2}{m_X^2}\right) + \frac{m_\mu^2}{m_X^2} x} \simeq 8.64 \times 10^{-3} (h'_\mu)^2, \quad (38)$$

$$\Delta a_\mu^{(A)} = -\frac{h_\mu^2}{4\pi^2} \frac{m_\mu^2}{m_X^2} \int_0^1 dx \frac{x^3}{(1-x)\left(1 - \frac{m_\mu^2}{m_X^2}\right) + \frac{m_\mu^2}{m_X^2} x} \simeq -1.19 \times 10^{-3} h_\mu^2. \quad (39)$$

Thus a vector $X17$ *raises* a_μ (positive sign), while a pseudoscalar *lowers* it (negative sign).

Using the latest experimental world average from the Muon $g-2$ experiment at Fermilab [23], we take

$$a_\mu^{\text{exp}} = 116\,592\,070.5(14.5) \times 10^{-11}. \quad (40)$$

For the Standard-Model prediction we use the 2025 update by the Muon $g-2$ Theory Initiative [24],

$$a_\mu^{\text{SM}} = 116\,592\,033(62) \times 10^{-11}. \quad (41)$$

These imply

$$\Delta a_\mu \equiv a_\mu^{\text{exp}} - a_\mu^{\text{SM}} = 3.8(6.3) \times 10^{-10}. \quad (42)$$

It is important to note that this discrepancy represents only a 0.6σ deviation, largely due to the 2025 Theory Initiative's adoption of lattice-QCD results for the hadronic vacuum polarization (HVP) contribution. This marks a significant shift from the earlier $\sim 4\sigma$ tension reported by the 2020 Theory Initiative white paper, which relied primarily on dispersive evaluations. While the theoretical situation remains under active investigation—with ongoing efforts to reconcile the lattice and dispersive approaches—the current picture suggests substantially reduced room for new-physics contributions to the muon anomaly.

Nevertheless, for the purpose of this work, we adopt benchmark couplings that remain consistent with the $\pm 6\sigma$ envelope around the measured discrepancy. We denote by σ_a the one-sigma width for Δa_μ ,

$$\sigma_a \equiv 6.3 \times 10^{-10}. \quad (43)$$

Given the 2025 update of the Muon $g-2$ Theory Initiative, which adopts a consolidated lattice-QCD average for the LO-HVP contribution, the current difference corresponds to only a $\sim 0.6\sigma$ effect and is therefore statistically consistent with zero at the present precision. In this situation, our goal is not to provide a best-fit explanation of the muon anomaly, but rather to define representative upper-scale benchmark couplings for assessing the potential size of $X17$ -induced atomic shifts and their systematic uncertainties. We therefore allow Δa_μ to vary within a wide interval $\Delta a_\mu \pm 6\sigma_a$, which avoids imposing a strong prior on the unsettled HVP treatment and prevents overly restrictive benchmark couplings that would trivially suppress the signal. Since all $X17$ -induced energy shifts considered here scale as h_μ^2 (or $(h'_\mu)^2$), our results can be straightforwardly rescaled to any narrower confidence interval if desired.

To define benchmark targets reflecting the current situation, in which the experimental central value lies above the SM prediction by $+0.6\sigma$, we choose

$$\Delta a_\mu^{(V)} = +0.6 \sigma_a = +3.78 \times 10^{-10}, \quad \Delta a_\mu^{(A)} = -(6.0 - 0.6) \sigma_a = -5.4 \sigma_a = -3.402 \times 10^{-9}. \quad (44)$$

Inserting these targets into Eqs. (38)–(39), the benchmark muon-side couplings are

$$h'_\mu = 2.09 \times 10^{-4}, \quad (45)$$

$$h_\mu = -1.69 \times 10^{-3}. \quad (46)$$

These benchmark choices should not be interpreted as statistically preferred fits. Rather, they serve as representative upper-scale couplings consistent with the sign of the one-loop contributions and with the broadened $\pm 6\sigma$ range adopted in this work.

D. Nuclear structure and magnetic response for $Z \leq 15$ nuclei

In light nuclei ($Z \leq 15$) the independent-particle shell model provides a quantitatively successful zeroth-order description of ground-state spins and magnetic moments [15, 16, 25, 26]. Pauli blocking fills the lowest single-particle orbitals in time-reversed pairs, so their spin contributions cancel and the net magnetic and spin-dependent response is dominated by the unpaired valence nucleon(s) in the open shell [13, 27].

We parameterize the nucleon-side coupling of an $X17$ mediator to a given nucleus through spin fractions $\Delta_{p,n}$ that encode the proton/neutron share of the nuclear spin:

$$\Delta_{p,n} \equiv \frac{\langle \sum_{i \in p,n} \mathbf{S}_i \rangle \cdot \hat{\mathbf{I}}}{\hbar I}, \quad \langle \sum_{i \in p,n} \mathbf{S}_i \rangle = \alpha_{ij}^{(S)} \hbar \hat{\mathbf{I}}. \quad (47)$$

Here I and $\hat{\mathbf{I}}$ are the nuclear spin magnitude and its unit vector. For a single Schmidt nucleon with orbital angular momentum l and total angular momentum $j = l \pm \frac{1}{2}$, the spin-projection coefficient is

$$\alpha_{ij}^{(S)} = \frac{j(j+1) + s(s+1) - l(l+1)}{2(j+1)}, \quad s = \frac{1}{2}. \quad (48)$$

For even-even ($I=0$) nuclei, $\Delta_p = \Delta_n = 0$ by definition.

When both a valence proton and a valence neutron contribute to the ground-state spin (odd-odd nuclei), their angular momenta j_p and j_n couple to the total I in the weak-coupling limit. The projection coefficients are

$$C_p = \frac{I(I+1) + j_p(j_p+1) - j_n(j_n+1)}{2I(I+1)}, \quad C_n = \frac{I(I+1) + j_n(j_n+1) - j_p(j_p+1)}{2I(I+1)}, \quad (49)$$

$$\Delta_p = \frac{C_p \alpha_{l_p j_p}^{(S)}}{I}, \quad \Delta_n = \frac{C_n \alpha_{l_n j_n}^{(S)}}{I}. \quad (50)$$

These reproduce the standard additivity formulas used in nuclear magnetic-moment systematics [13, 15, 27]; for odd- A nuclei the expressions reduce to the single-Schmidt form.

Given $\Delta_{p,n}$, the effective nucleon-side couplings entering the $X17$ -induced hyperfine operators are

$$h_N^{(\text{eff})} = h'_p \Delta_p + h'_n \Delta_n \quad (\text{vector HFS}), \quad h_N^{(\text{eff})} = h_p \Delta_p + h_n \Delta_n \quad (\text{pseudoscalar HFS}). \quad (51)$$

These effective couplings enter exclusively the $X17$ -induced hyperfine operators of Eqs. (7)–(8). For the vector-induced $2S_{1/2} - 2P_{1/2}$ Lamb shift, the relevant muon–nucleus coupling is instead the coherent sum $Zh'_p + Nh'_n$ appearing in Eq. (6), which probes the total spin-independent vector charge of the nucleus rather than its spin content. The numerical values of both $h_N^{(\text{eff})}$ and $Zh'_p + Nh'_n$ for each nuclide are listed in Appendix A 2.

We illustrate the procedure with three representative p -shell nuclei, whose single-particle occupancies are shown in Fig. 2. For ^{13}C ($Z=6$, $N=7$, $I^\pi = \frac{1}{2}^-$), the valence neutron occupies $1p_{1/2}$; Eq. (48) gives $\alpha_{p_{1/2}}^{(S)} = -\frac{1}{6}$, so that $\Delta_n = -\frac{1}{3}$ and $\Delta_p = 0$. For ^{14}N ($Z=7$, $N=7$, $I^\pi = 1^+$), two valence nucleons with $j_p = j_n = \frac{1}{2}$ occupy $1p_{1/2}$; Eq. (49) yields $C_p = C_n = \frac{1}{2}$, and with $I = 1$ one finds $\Delta_p = \Delta_n = -\frac{1}{12}$. For ^{15}N ($Z=7$, $N=8$, $I^\pi = \frac{1}{2}^-$), the neutron p shell is closed and the valence proton occupies $1p_{1/2}$, giving $\Delta_p = -\frac{1}{3}$ and $\Delta_n = 0$.

Configuration mixing and core polarization modify these Schmidt-model values at a level that depends sensitively on the nuclear structure of each isotope and is not uniformly well-constrained [13, 16, 27]. The orbital assignments and spin-projection coefficients adopted throughout this work are used solely to define a consistent Schmidt-model baseline for the survey, and should not be interpreted as a claim of a full shell-model description. This baseline

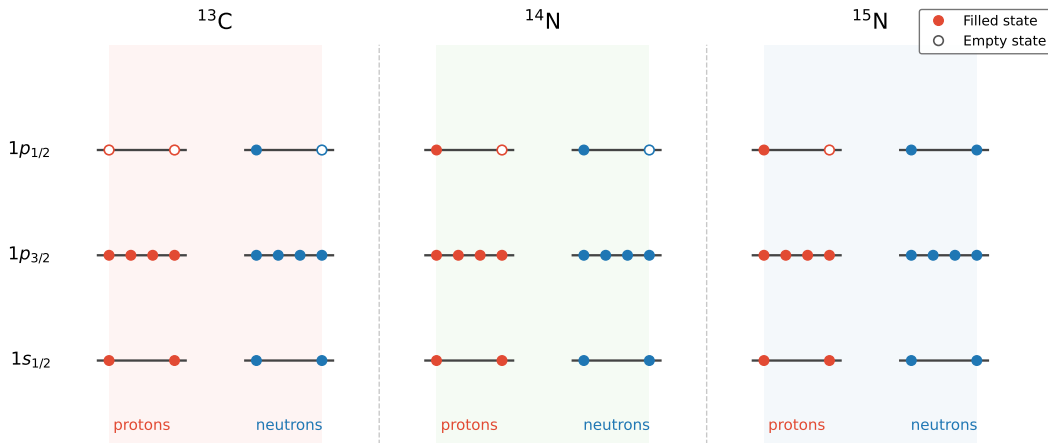


FIG. 2. Single-particle occupancies in the p shell for ^{13}C , ^{14}N , and ^{15}N . The $1s_{1/2}$, $1p_{3/2}$, and $1p_{1/2}$ orbitals are shown; left (right) columns correspond to proton (neutron) states. Filled circles denote occupied states.

is sufficient for the purpose of identifying the relative $X17$ -sensitivity trends across the nuclear chart; quantitative precision for the highest-priority targets will require beyond-Schmidt calculations.

Unless otherwise noted, ground-state J^π assignments and low-lying level energies are taken from the evaluated databases TUNL [28] and ENSDF (accessed via NNDC NuDat3) [29]; for isotonic-chain cross-checks we consult the KAERI chart of nuclides [30]. Shape information motivating Nilsson assignments is supported by evaluated electric quadrupole moments [31] and the Bohr-Mottelson rotational-coupling formalism [16]. For the $N=11$ isotones we adopt ^{21}Ne as prolate with $I^\pi = \frac{3}{2}^+$ and the first $5/2^+$ level at $E \simeq 351$ keV [29–31].

The experimental nuclear g -factors are computed from evaluated magnetic moments and spins via

$$g_N^{(\text{exp})} = \frac{m_{\text{nuc}}}{m_p} \frac{\mu_{\text{exp}}}{\mu_N I}, \quad (52)$$

where μ_{exp} is expressed in nuclear magnetons $\mu_N = e\hbar/(2m_p c)$ and the factor m_{nuc}/m_p enforces the convention of Eq. (5). Nuclear masses are from AME2020 [12]; magnetic moments for the light nuclei ^1H , ^2H , ^3H , ^3He are taken from PDG [32], and those for stable nuclides with $Z \leq 15$ from Stone's evaluated tables [13, 31].

E. Validation and systematic uncertainties

Before presenting predictions for $X17$ -induced shifts, we assess the robustness of the theoretical framework against two sources of systematic error: higher-order QED corrections to the wave function, and the point-nucleus approximation for the Uehling potential.

a. Finite-size Uehling correction. The Uehling potential in Eq. (4) was derived for a point nucleus. For nuclei with finite charge radius R_{ch} , the proper treatment convolves the point-nucleus potential with the nuclear charge distribution [33, 34]:

$$V_{\text{Ueh}}^{(\text{fs})}(\mathbf{r}) = \int \frac{\rho_{\text{ch}}(\mathbf{r}')}{Z} V_{\text{Ueh}}^{(\text{pt})}(|\mathbf{r} - \mathbf{r}'|) d^3\mathbf{r}', \quad (53)$$

where $V_{\text{Ueh}}^{(\text{pt})}(r)$ is given by Eq. (4) and ρ_{ch} satisfies $\int \rho_{\text{ch}} d^3r' = Z$. Adopting a uniformly charged sphere of radius R_{ch} ,

$$\rho_{\text{ch}}(r') = \begin{cases} \frac{3Z}{4\pi R_{\text{ch}}^3}, & r' \leq R_{\text{ch}}, \\ 0, & r' > R_{\text{ch}}, \end{cases} \quad (54)$$

the angular integration reduces to [34]

$$V_{\text{Ueh}}^{(\text{fs})}(r) = \frac{2\pi}{r} \int_0^\infty \frac{\rho_{\text{ch}}(r')}{Z} r'^2 dr' \int_{|r-r'|}^{r+r'} V_{\text{Ueh}}^{(\text{pt})}(s) s ds, \quad (55)$$

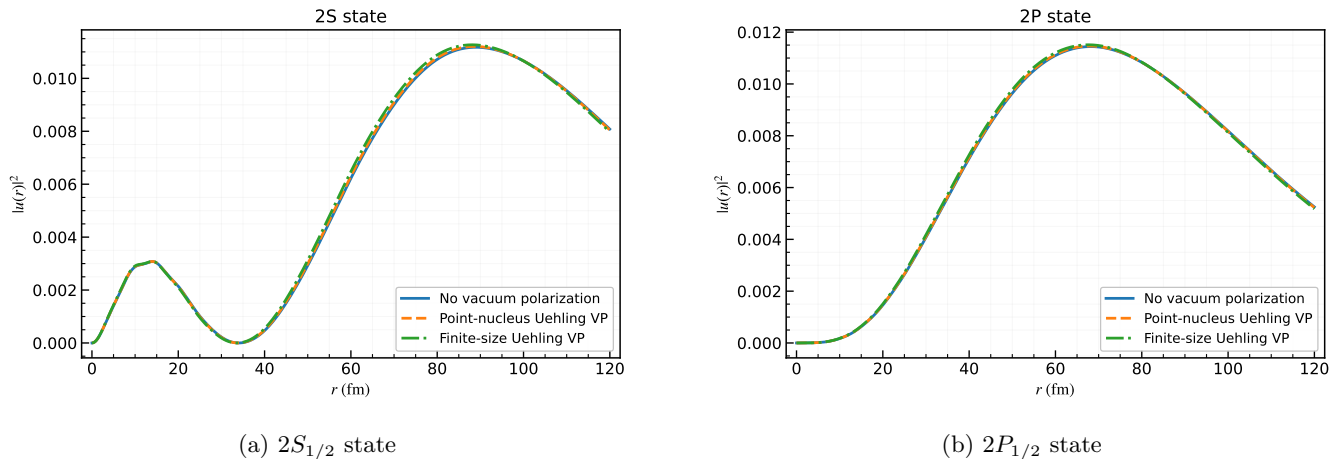


FIG. 3. Radial probability densities for the $2S_{1/2}$ and $2P_{1/2}$ states of muonic ^{31}P under three QED treatments: no vacuum polarization, point-nucleus Uehling potential, and finite-size Uehling potential. Even for ^{31}P , the heaviest system considered in the present validation test, the three curves are nearly indistinguishable, showing that the finite-size Uehling correction does not affect the qualitative conclusions of the survey.

which is evaluated numerically on the GEM radial mesh.

To quantify the impact of this correction, we compare the radial probability densities $|u(r)|^2 = r^2|\psi(r)|^2$ for the $2S_{1/2}$ and $2P_{1/2}$ states of $\mu^{31}\text{P}$ ($Z = 15$, $R_{\text{ch}} = 3.19$ fm [14]) under three levels of approximation: (i) no vacuum polarization; (ii) point-nucleus Uehling; and (iii) finite-size Uehling from Eq. (55). As shown in Fig. 3, the three curves are numerically indistinguishable across the full radial range, including the region $r \lesssim m_X^{-1} \approx 12$ fm where the $X17$ Yukawa potential is most concentrated. The finite-size Uehling correction is known to be negligible for light nuclei and to grow only for $Z \gtrsim 20$ [35]; ^{31}P at $Z = 15$ therefore represents the most demanding case in our survey. We conclude that the point-nucleus approximation is unlikely to alter the ranking of optimal targets or the qualitative conclusions of the survey for any nucleus in our range. Similarly, folding the short-range $X17$ Yukawa potential with the nuclear density distribution ρ_{ch} would introduce corrections for the heaviest nuclei ($Z \sim 15$); we leave the evaluation of this folded Yukawa potential to future precision studies, as it falls within the current margin of nuclear-structure uncertainties.

b. Higher-order QED effects. Beyond the leading Uehling term, the Lamb shift in muonic atoms receives contributions from the Källén–Sabry two-loop vacuum polarization, the Wichmann–Kroll self-energy correction, and hadronic vacuum polarization. These are collectively known to contribute at the level of ~ 0.01 – 0.1% of the total Lamb shift in light muonic atoms [35, 36]. Because these corrections arise from loop insertions on the photon propagator, they modify the overall energy scale without introducing length scales comparable to $m_X^{-1} \approx 12$ fm. Their effect on the short-range wave-function amplitude—which governs the $X17$ -induced hyperfine shifts—is therefore expected to remain subleading for the purpose of target identification, and is unlikely to alter the ranking of optimal candidates relative to the nuclear-spin uncertainty discussed below.

c. Nuclear-structure uncertainties. The dominant theoretical uncertainty in the $X17$ -induced hyperfine shifts derives from the Schmidt-model treatment of nuclear spin content, rather than from QED corrections to the wave function. Configuration mixing and core polarization can shift the effective spin fractions $\Delta_{p,n}$ by amounts that are nucleus-dependent and not uniformly constrained [13, 16, 27]. Since our primary goal is to identify the most sensitive experimental targets rather than to make definitive quantitative predictions, this limitation does not affect the principal conclusions of the survey.

III. RESULTS AND EXPERIMENTAL PROSPECTS

A. Benchmark validation of the GEM framework

Before presenting the $X17$ -induced signals, we benchmark the GEM framework in two complementary ways. First, we compare the electromagnetic baseline energies with published high-precision QED results. Second, we compare the dimensionless $X17$ -induced hyperfine ratio E_X/E_F with the analytic estimates of Jentschura [8] for μp and μd . The results are summarized in Table V.

TABLE V. GEM results benchmarked against published calculations. *Upper block*: electromagnetic level energies vs. high-precision QED; reference values from Faustov & Martynenko [37] (1S HFS in μp), Faustov, Martynenko et al. [38] (1S HFS in μd), Martynenko [39] (1S HFS in $\mu^3\text{He}^+$), Borie [35] (Lamb shift in μp , total with $R_p = 0.875$ fm), Krutov & Martynenko [40] (Lamb shift in μd). *Lower block*: dimensionless X17-to-Fermi ratio E_X/E_F for the $1S_{1/2}$ HFS vs. the analytic estimates of Jentschura [8] [Eq. (56)], evaluated with the coupling parameters adopted in this work. EM deviations: $\delta = |E_{\text{GEM}} - E_{\text{ref}}|/|E_{\text{ref}}| \times 100\%$.

Observable	System	E_{GEM}	E_{ref}	δ [%]	Reference
<i>Electromagnetic baseline (energies in meV)</i>					
$1S_{1/2}$ HFS	μp	183.235	182.638	0.33	[37]
	μd	49.644	48.584	2.18	[38]
	$\mu^3\text{He}^+$	1377.59	1334.56	3.22	[39]
Lamb shift $ E(2S_{1/2}) - E(2P_{1/2}) $	μp	198.677	202.05*	1.67	[35]
	μd	198.837	202.414	1.77	[40]
<i>X17-to-Fermi ratio E_X/E_F</i>					
Vector X17, $1S_{1/2}$	μp	5.6×10^{-7}	3.3×10^{-8}	‡	Eq. (56)a
	μd	3.8×10^{-6}	1.4×10^{-6}	‡	Eq. (56)a
Pseudoscalar X17, $1S_{1/2}$	μp	4.7×10^{-6}	1.3×10^{-6}	‡	Eq. (56)b
	μd	3.6×10^{-6}	4.5×10^{-6}	‡	Eq. (56)b

* Evaluated from Borie's parameterization $\Delta E_{LS} = 206.060 - 5.2794\langle r^2 \rangle + 0.0546\langle r^2 \rangle^{3/2}$ meV with $R_p = 0.875$ fm ($\langle r^2 \rangle = 0.7656$ fm²).

‡ Both the GEM numerical ratios and the reference values are evaluated with the coupling parameters adopted in this work. The residual factor-of-2–10 discrepancies arise from the approximations in the analytic formula (Eq. (30) of Ref. [8]), which retains only the leading contact-term limit $\sim \delta^{(3)}(\mathbf{r})$, whereas GEM integrates the full Yukawa radial profile $e^{-m_X r}/r$. This order-of-magnitude agreement validates the correct implementation of the X17–nucleon interaction in the GEM Hamiltonian.

$E_F = E_{\text{HFS}}^{\text{GEM}}/4$ (spin- $\frac{1}{2}$) or $E_{\text{HFS}}^{\text{GEM}}/6$ (spin-1 deuteron).

For the electromagnetic baseline, the agreement degrades gradually with increasing nuclear complexity: the deviation in the $1S_{1/2}$ hyperfine splitting grows from 0.33% in μp to 2.18% in μd and 3.22% in $\mu^3\text{He}^+$. This trend is consistent with the increasing importance of higher-order nuclear-structure effects, such as Zemach, polarizability, and relativistic recoil corrections, which are included in the reference calculations [37–39] but not in the present Hamiltonian. For the Lamb shift, both μp and μd show a systematic deficit of about 3.4 meV ($\sim 1.7\%$), which can be attributed mainly to missing higher-order vacuum-polarization and recoil contributions.

The lower block of Table V tests the new-physics sector by comparing the numerical ratio $E_X/E_F \equiv \Delta E^{X17}/E_{\text{Fermi}}$ with the leading-order analytic estimates of Jentschura [8],

$$\frac{E_{X,V}(nS_{1/2})}{E_F(nS_{1/2})} \approx -\frac{2h'_\mu h'_N}{g_N \pi} \frac{Zm_r}{m_X}, \quad (56a)$$

$$\frac{E_{X,A}(nS_{1/2})}{E_F(nS_{1/2})} \approx \frac{h_\mu h_N}{g_N \pi} \frac{Zm_r}{m_X}. \quad (56b)$$

The agreement is at the order-of-magnitude level, as expected, since the analytic expressions retain only the leading contact-term limit, whereas the GEM calculation includes the full Yukawa radial profile. This comparison confirms that the X17 interaction has been implemented correctly in the numerical framework.

Overall, for the benchmark systems μp , μd , and $\mu^3\text{He}^+$, the GEM reproduces the electromagnetic observables at the 0.3–3% level, which is sufficient for the purpose of target identification. For heavier systems in the survey, analogous high-precision benchmarks are not available, but the omitted higher-order QED contributions are expected to remain too small to alter the ranking of optimal candidates. The dominant theoretical uncertainty therefore comes from the Schmidt-model treatment of nuclear spin content rather than from the GEM baseline itself.

B. Vector-induced $2S_{1/2}$ - $2P_{1/2}$ Lamb shifts

A vector $X17$ mediator induces a spin-independent Yukawa potential through the coherent nuclear coupling

$$V_X(r) = \frac{h'_\mu}{4\pi} (Zh'_p + Nh'_n) \frac{e^{-m_X r}}{r}. \quad (57)$$

This interaction shifts the level centroids, with the largest effect occurring for S states whose wave functions probe the nuclear region most strongly. In contrast to the hyperfine sector, where the relevant couplings are weighted by the spin-carrying valence nucleon(s), the Lamb shift depends on the fully coherent combination $Zh'_p + Nh'_n$. Because the protophobic benchmark implies $h'_n \gg h'_p$, the vector-induced Lamb-shift signal increases strongly toward neutron-rich and heavier nuclei.

We define

$$\Delta E_{X17}^{(V)} \equiv E_{X17}^{(V)}(2S_{1/2}) - E_{X17}^{(V)}(2P_{1/2}) \quad (58)$$

and use its absolute value as the experimentally relevant quantity. The full results for all stable nuclei with $Z \leq 15$ are listed in Appendix B and shown in Fig. 4.

A clear systematic pattern emerges across the nuclear chart. In the lightest systems, the signal increases rapidly from hydrogenic to helium systems: $|\Delta E_{X17}^{(V)}| = 2.05 \times 10^{-3}$ meV for μp , 3.20×10^{-2} meV for μd , 0.245 meV for $\mu^3\text{He}^+$, and 0.468 meV for $\mu^4\text{He}^+$. This growth reflects both the increasing short-distance wave-function amplitude and the coherent enhancement from the nuclear coupling.

Unlike hyperfine observables, the vector Lamb shift is not restricted to nuclei with nonzero spin. As a result, even-even nuclei become fully competitive and often dominant, although the strongest case in the present survey is an odd- Z system. Large shifts are found already in $\mu^{12}\text{C}$ (21.2 meV), $\mu^{13}\text{C}$ (24.5 meV), $\mu^{16}\text{O}$ (50.4 meV), $\mu^{18}\text{O}$ (62.1 meV), $\mu^{20}\text{Ne}$ (94.2 meV), $\mu^{24}\text{Mg}$ (150 meV), $\mu^{26}\text{Mg}$ (174 meV), $\mu^{28}\text{Si}$ (174 meV), and $\mu^{30}\text{Si}$ (197 meV). The target hierarchy is therefore governed primarily by coherent charge enhancement and radial overlap, rather than by nuclear spin structure.

The p -shell nuclei form an intermediate region between the tiny hydrogenic signals and the much larger sd -shell shifts. In particular, $\mu^9\text{Be}$, $\mu^{10}\text{B}$, $\mu^{11}\text{B}$, and $\mu^{13}\text{C}$ yield 6.92, 11.84, 14.06, and 24.5 meV, respectively, while $\mu^6\text{Li}$ and $\mu^7\text{Li}$ give 2.06 and 2.71 meV.

The strongest vector-induced Lamb-shift signal in the survey is obtained for $\mu^{31}\text{P}$, with $|\Delta E_{X17}^{(V)}| = 264$ meV. The next strongest case is $\mu^{29}\text{Si}$ (237 meV), followed by $\mu^{30}\text{Si}$ (197 meV), $\mu^{27}\text{Al}$ (195.5 meV), $\mu^{28}\text{Si}$ (174 meV), $\mu^{26}\text{Mg}$ (174 meV), $\mu^{25}\text{Mg}$ (161.7 meV), and $\mu^{24}\text{Mg}$ (150 meV), with $\mu^{21}\text{Ne}$ still reaching 102.9 meV. Although the ratio $|\Delta E_{X17}^{(V)}|/|\Delta E_L^{(\text{EM})}|$ decreases with increasing Z , because the ordinary Lamb shift grows even faster, the absolute $X17$ signal continues to rise over much of the survey range.

By contrast, a pseudoscalar $X17$ does not shift the spin-averaged level centroids at leading order, since its interaction is purely spin dependent and therefore averages to zero in the unpolarized $2S$ and $2P$ centroids. The Lamb shift is therefore a particularly clean probe of the vector hypothesis.

C. $1S_{1/2}$ hyperfine signatures

The $1S_{1/2}$ hyperfine splitting probes the spin structure of both the muon and the nucleus, and therefore accesses coupling combinations that are distinct from those entering the spin-independent Lamb shift. The full numerical results are listed in Appendices C and D, and the main trends are summarized in Fig. 5.

For $1S$ states, the dominant $X17$ contribution arises from the short-range contact term and therefore scales with the wave-function density at the origin,

$$|\psi_{1S}(0)|^2 \propto Z^3 m_r^3 \quad (59)$$

The overall size of the signal is then controlled by the effective nucleon-side couplings, which depend on the nuclear spin fractions Δ_p and Δ_n . Unlike the vector Lamb shift, the hyperfine sector is therefore intrinsically sensitive to nuclear spin structure and restricted to non-even-even nuclei.

For a vector mediator, the relevant effective coupling is

$$h'_N^{(\text{eff})} = h'_p \Delta_p + h'_n \Delta_n.$$

Because $h'_n \gg h'_p$ in the protophobic benchmark adopted here, the hierarchy is driven mainly by neutron spin content, and odd- N nuclei are strongly favored. The largest $1S_{1/2}$ hyperfine signal in the survey is found in $\mu^{29}\text{Si}$,

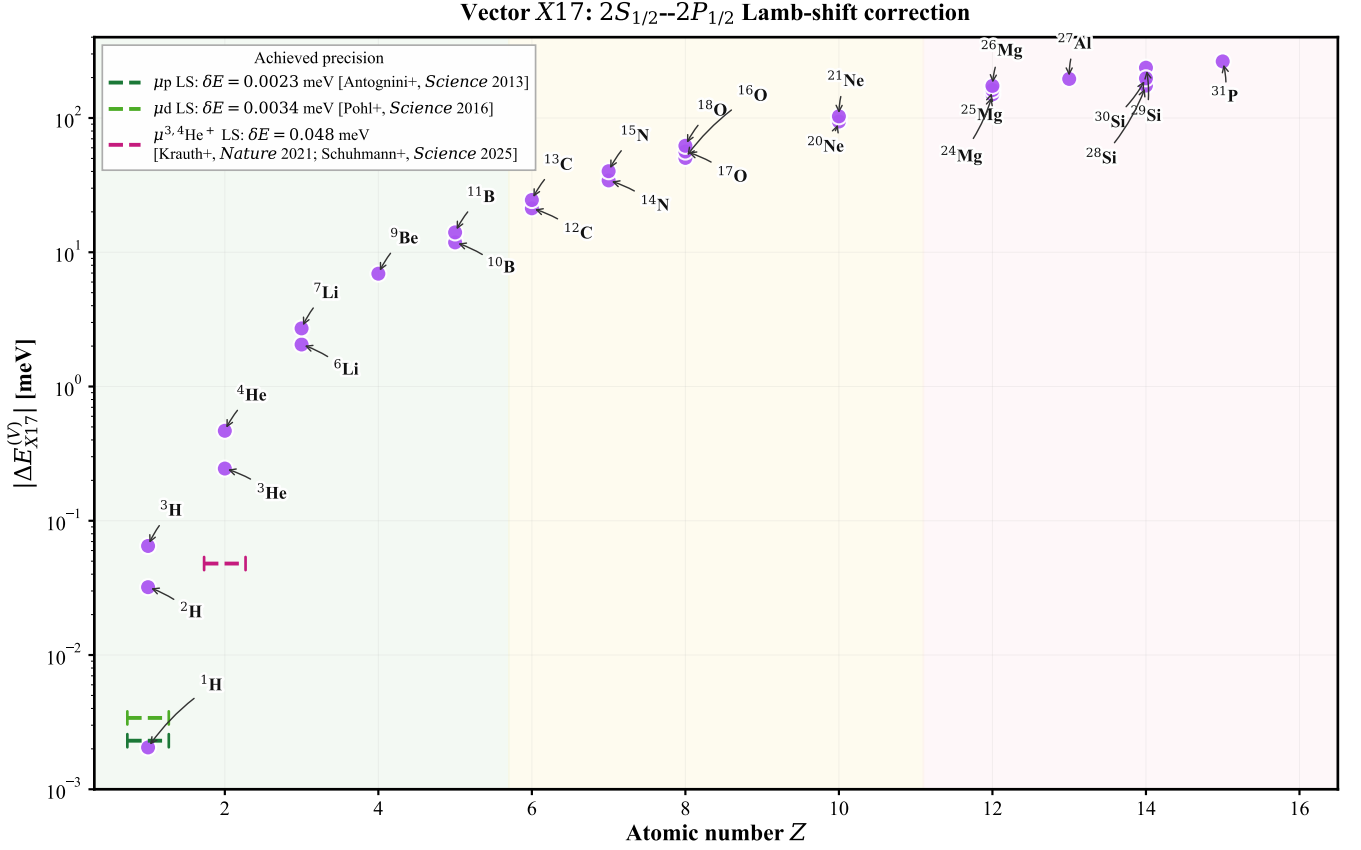


FIG. 4. Vector-X17 contribution to the $2S_{1/2} \rightarrow 2P_{1/2}$ Lamb shift for stable muonic atoms with $Z \leq 15$. The signal grows systematically toward heavier nuclei and reaches its largest value in $\mu^{31}\text{P}$ (264 meV).

where $|\Delta E_{X17}^{(V)}| = 0.643$ meV. This case combines a relatively large short-distance wave-function amplitude with maximal neutron-spin sensitivity ($\Delta_n = 1$, $\Delta_p = 0$). Other notable vector cases include $\mu^{31}\text{P}$, $\mu^{27}\text{Al}$, $\mu^{25}\text{Mg}$, and $\mu^{17}\text{O}$, although all remain well below the leading $\mu^{29}\text{Si}$ signal.

For a pseudoscalar mediator, the effective coupling becomes

$$h_N^{(\text{eff})} = h_p \Delta_p + h_n \Delta_n,$$

and the hierarchy is reversed because the proton-side coupling dominates, $|h_p| \gg |h_n|$. The pseudoscalar $1S_{1/2}$ hyperfine channel therefore selects odd- Z nuclei. The strongest signal is obtained in $\mu^{31}\text{P}$, with $|\Delta E_{X17}^{(A)}| = 0.710$ meV, followed at a much lower level by $\mu^{27}\text{Al}$ at 0.053 meV. In $\mu^{31}\text{P}$, the valence proton occupies the $2s_{1/2}$ orbital, giving $\Delta_p = 1$ and $\Delta_n = 0$, which maximizes the pseudoscalar response.

The complementarity between the two hypotheses is therefore especially clear in the $1S_{1/2}$ hyperfine sector: odd- N nuclei dominate in the vector case, whereas odd- Z nuclei dominate in the pseudoscalar case. This provides a natural discriminator between mediator scenarios.

D. $2P_{1/2}$ hyperfine signatures

The $2P_{1/2}$ hyperfine corrections, shown in Fig. 6 and tabulated in Appendices C2 and D2, follow the same qualitative selectivity as their $1S_{1/2}$ counterparts, but are much smaller throughout the survey.

This suppression has two main origins. First, the P -state wave function vanishes at the origin, so the short-range contact contribution that dominates the $1S_{1/2}$ hyperfine splitting is strongly reduced. Since the Yukawa interaction probes mainly the region $r \lesssim m_X^{-1} \approx 12$ fm, the resulting $2P_{1/2}$ shifts are suppressed by several orders of magnitude relative to the corresponding $1S_{1/2}$ values. For the lightest systems, the vector-induced $2P_{1/2}$ correction is already of order 10^{-9} meV.

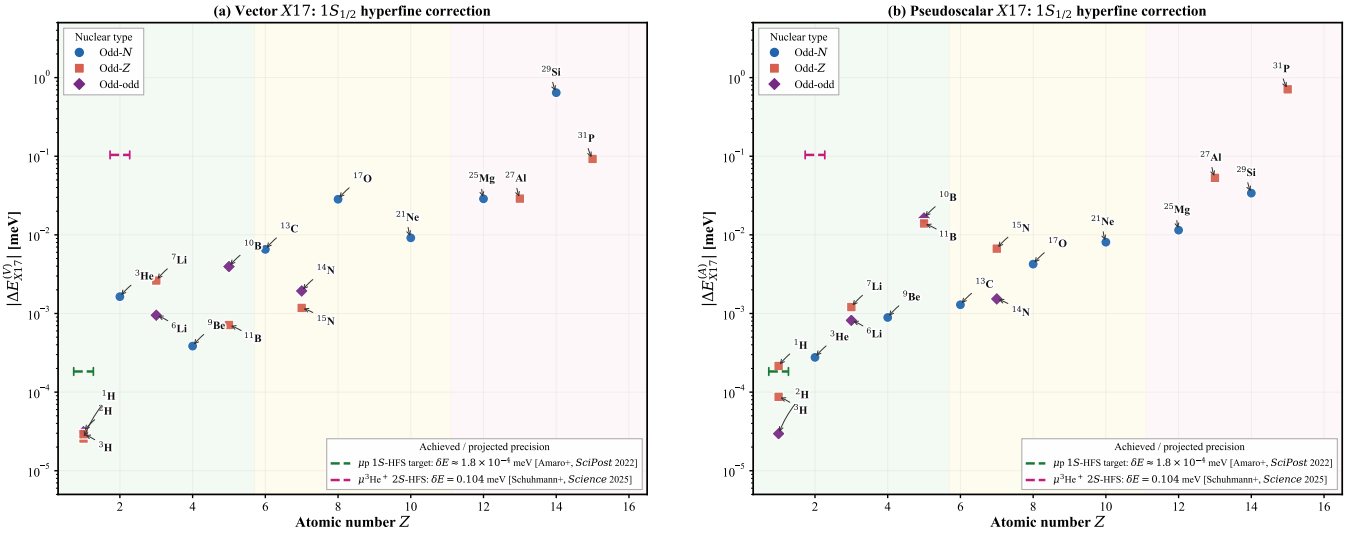


FIG. 5. $X17$ -induced $1S_{1/2}$ hyperfine corrections for stable muonic atoms with $Z \leq 15$: (a) vector mediator and (b) pseudoscalar mediator. The vector case preferentially enhances odd- N nuclei, while the pseudoscalar case favors odd- Z nuclei. The largest signals are found in $\mu^{29}\text{Si}$ (0.643 meV) and $\mu^{31}\text{P}$ (0.710 meV), respectively.

Second, the $2P_{1/2}$ hyperfine operator contains tensor and spin-orbit terms in addition to the reduced contact contribution, and these terms partially cancel in many nuclei. An especially striking example is ^{15}N , for which the vector-induced correction is only $|\Delta E_{X17}^{(V)}(2P_{1/2})| \simeq 5.9 \times 10^{-10}$ meV because of an almost complete cancellation among the relevant sublevel contributions.

Despite the strong suppression, the overall hierarchy remains consistent with the $1S_{1/2}$ hyperfine sector. In the vector case, odd- N nuclei still dominate, with $\mu^{29}\text{Si}$ giving the largest $2P_{1/2}$ signal, $|\Delta E_{X17}^{(V)}| = 8.70 \times 10^{-4}$ meV. In the pseudoscalar case, odd- Z nuclei remain favored, with $\mu^{31}\text{P}$ reaching $|\Delta E_{X17}^{(A)}| = 5.39 \times 10^{-4}$ meV. The persistence of the same nuclear selectivity in both the $1S_{1/2}$ and $2P_{1/2}$ channels provides an internal consistency check on the coupling pattern.

In absolute size, however, all $2P_{1/2}$ hyperfine shifts remain far below the $1S_{1/2}$ signals. We therefore include them mainly for completeness and for future theoretical cross-checks; their relevance for experimental target selection is limited.

E. Identification of optimal experimental targets

Table VI summarizes the most relevant candidate systems for the three experimentally meaningful observable-hypothesis combinations considered here: the vector- $X17$ Lamb shift, the vector- $X17$ $1S_{1/2}$ hyperfine splitting, and the pseudoscalar- $X17$ $1S_{1/2}$ hyperfine splitting. For each channel, we list both the leading theoretical candidates ranked by signal size and the light systems for which precision benchmarks already exist. The $2P_{1/2}$ hyperfine channel is not included, since its predicted signals remain far below current or foreseeable experimental sensitivity.

Among systems with demonstrated precision spectroscopy, the most promising near-term probes of the vector-induced Lamb shift are μd , $\mu^3\text{He}^+$, and $\mu^4\text{He}^+$. Their predicted signals reach $|\Delta E_{X17}^{(V)}| = 3.20 \times 10^{-2}$ meV, 0.245 meV, and 0.468 meV, corresponding to $\mathcal{R} \simeq 9.4$, 5.1, and 9.8, respectively, relative to existing or demonstrated precision scales. These systems therefore offer the most direct near-term experimental access to the vector Lamb-shift channel.

Beyond the light benchmark systems, the largest absolute vector Lamb-shift signals are found in the upper part of the present survey range. The strongest case is $\mu^{31}\text{P}$, with $|\Delta E_{X17}^{(V)}| = 264$ meV, followed by $\mu^{29}\text{Si}$, $\mu^{30}\text{Si}$, $\mu^{27}\text{Al}$, $\mu^{28}\text{Si}$, $\mu^{26}\text{Mg}$, and $\mu^{25}\text{Mg}$. Although no meV-level spectroscopy benchmark yet exists for these nuclei, their large predicted signals make them natural targets for future dedicated programs. Between the light benchmark systems and these largest signals lies an intermediate group—notably $\mu^9\text{Be}$, $\mu^{10}\text{B}$, $\mu^{11}\text{B}$, and $\mu^{13}\text{C}$ —which may serve as useful stepping stones for future experimental development.

For hyperfine observables, the leading long-term targets remain $\mu^{29}\text{Si}$ for the vector scenario and $\mu^{31}\text{P}$ for the pseudoscalar scenario. The corresponding $1S_{1/2}$ signals are 0.643 meV and 0.710 meV, respectively, and are the

$2P_{1/2}$ hyperfine corrections: magnitudes well below current experimental reach

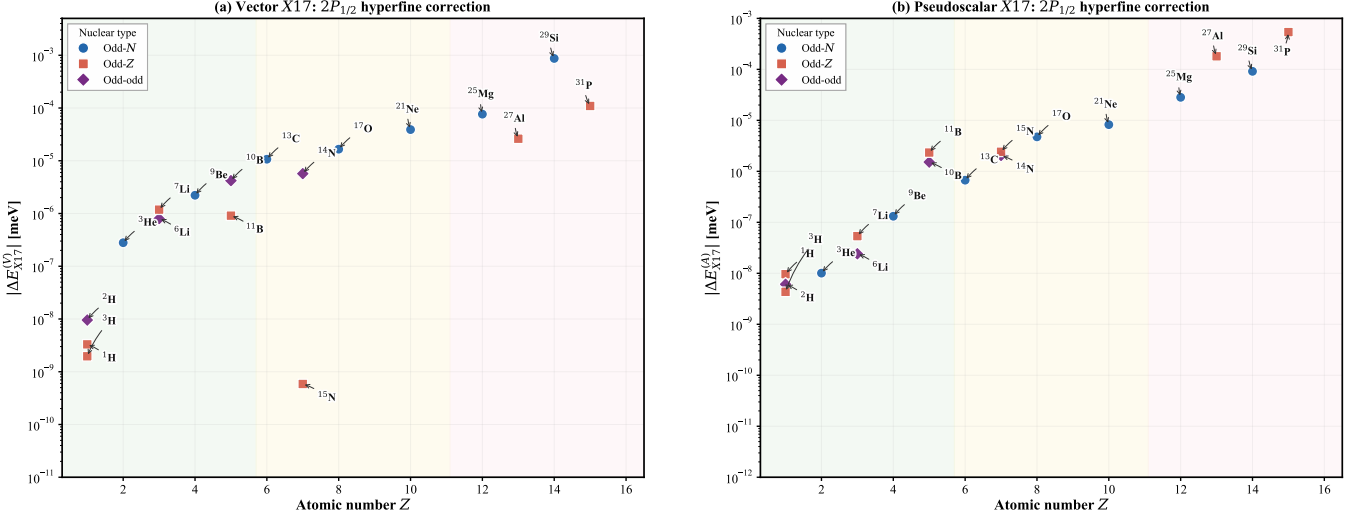


FIG. 6. $X17$ -induced $2P_{1/2}$ hyperfine corrections for stable muonic atoms with $Z \leq 15$: (a) vector mediator and (b) pseudoscalar mediator. Compared with the corresponding $1S_{1/2}$ channel, the corrections are strongly suppressed. The largest signals are obtained in $\mu^{29}\text{Si}$ for the vector case and $\mu^{31}\text{P}$ for the pseudoscalar case.

largest hyperfine effects found in the survey. More generally, the target pattern is strongly complementary: odd- N nuclei are favored in the vector case, whereas odd- Z nuclei dominate in the pseudoscalar case.

Muonic hydrogen remains an important benchmark. In the vector Lamb-shift channel, the predicted signal in μp , $|\Delta E_{X17}^{(V)}| = 2.05 \times 10^{-3}$ meV, lies slightly below the achieved CREMA precision, corresponding to $\mathcal{R} = 0.89$. By contrast, in the pseudoscalar $1S_{1/2}$ hyperfine channel, the μp signal reaches $|\Delta E_{X17}^{(A)}| = 2.15 \times 10^{-4}$ meV, giving $\mathcal{R} \simeq 1.2$ at the target precision of the ongoing PSI and RAL programs. These light systems therefore remain essential anchors for interpreting the heavier candidates.

Taken together, the present survey suggests a clear experimental hierarchy. For the vector Lamb-shift channel, the most immediate opportunities are provided by μd and the helium ions, where the predicted signals already exceed demonstrated precision benchmarks. For future dedicated programs, the largest absolute gains lie in the heaviest systems considered here, especially $\mu^{31}\text{P}$ and the silicon, aluminum, and magnesium isotopes. In the hyperfine sector, the complementary pair $\mu^{29}\text{Si}$ (vector) and $\mu^{31}\text{P}$ (pseudoscalar) stands out as the most informative combination for probing the spin-parity structure of a possible $X17$ mediator.

TABLE VI. Representative experimental targets and validation benchmarks for the X17 sensitivity survey in muonic atoms. For each observable–hypothesis combination, systems are listed in descending order of predicted signal size. The signal-to-precision ratio $\mathcal{R} \equiv |\Delta E_{X17}|/\delta E$ indicates whether a decisive test is feasible at the benchmark couplings adopted in this work. The $2P_{1/2}$ HFS channel is not included because its predicted signals remain far below current or foreseeable experimental sensitivity (see Sec. III D).

Observable	Nuclide	$ \Delta E_{X17} $ [meV]	δE [meV]	\mathcal{R}	Experimental context
<i>Vector X17: $2S_{1/2}$-$2P_{1/2}$ Lamb shift</i>					
	$\mu^{31}\text{P}$	264	—	—	next-gen, proposed
	$\mu^{29}\text{Si}$	237	—	—	next-gen, proposed
	$\mu^{30}\text{Si}$	197	—	—	next-gen, proposed
	$\mu^{27}\text{Al}$	196	—	—	next-gen, proposed
	$\mu^{28}\text{Si}$	174	—	—	next-gen, proposed
	$\mu^{26}\text{Mg}$	174	—	—	next-gen, proposed
	$\mu^4\text{He}^+$	0.468	0.048	9.75	[41]
	$\mu^3\text{He}^+$	0.245	0.048	5.10	[7]
	μd	3.20×10^{-2}	3.4×10^{-3}	9.42	[42]
	μp	2.05×10^{-3}	2.3×10^{-3}	0.89	[6]
<i>Vector X17: $1S_{1/2}$ hyperfine splitting</i>					
	$\mu^{29}\text{Si}$	0.643	—	—	next-gen pulsed muon [43]
	$\mu^{31}\text{P}$	0.092	—	—	next-gen pulsed muon [43]
	$\mu^{27}\text{Al}$	0.029	—	—	muonic X-ray spectroscopy
	$\mu^{25}\text{Mg}$	0.029	—	—	muonic X-ray spectroscopy
	$\mu^{17}\text{O}$	0.028	—	—	muonic X-ray spectroscopy
	$\mu^3\text{He}^+$	1.64×10^{-3}	0.104	0.016	[7]
	μp	2.57×10^{-5}	1.8×10^{-4}	0.14	[43]
<i>Pseudoscalar X17: $1S_{1/2}$ hyperfine splitting</i>					
	$\mu^{31}\text{P}$	0.710	—	—	next-gen pulsed muon [43]
	$\mu^{27}\text{Al}$	0.053	—	—	muonic X-ray spectroscopy
	$\mu^{10}\text{B}$	0.016	—	—	proposed, PSI
	$\mu^{11}\text{B}$	0.014	—	—	proposed, PSI
	$\mu^{15}\text{N}$	0.007	—	—	muonic X-ray spectroscopy
	$\mu^3\text{He}^+$	2.77×10^{-4}	0.104	0.003	[7]
	μp	2.15×10^{-4}	1.8×10^{-4}	1.2	[43]

IV. CONCLUSIONS

We have developed a systematic muonic-atom spectroscopy framework for probing short-range MeV-scale interactions, and applied it to a nucleus-by-nucleus survey of stable systems with $Z \leq 15$. The main conceptual advance is that spin-independent Lamb shifts and spin-dependent hyperfine splittings are treated on different and physically appropriate nuclear footings within the same atomic framework: the vector-induced Lamb shift is governed by the coherent muon–nucleus coupling $Zh'_p + Nh'_n$, whereas the hyperfine sector is built isotope by isotope from spin-fraction-weighted effective couplings. This observable-dependent construction makes it possible to expose, in a controlled way, the distinct nuclear systematics of vector and pseudoscalar mediators, and thereby turns comparative muonic spectroscopy from a collection of isolated case studies into a realistic target-selection strategy for new-physics searches.

A second important feature of the present work is that the benchmark muon-side couplings are chosen in accordance with the latest muon $g-2$ landscape. Rather than adopting benchmark scales motivated by the pre-2025 picture, we adopt benchmark couplings defined with reference to the final Fermilab measurement together with the 2025 Theory

Initiative update, for which the experimental–theoretical difference is substantially reduced. The resulting benchmarks should therefore not be viewed as preferred fits to a persistent anomaly, but as conservative and phenomenologically motivated reference scales for assessing the discovery reach of precision muonic spectroscopy.

Within this framework, several robust conclusions emerge. In the spin-independent channel, the vector-induced $2S_{1/2}$ – $2P_{1/2}$ Lamb-shift signal exhibits strong coherent enhancement and grows rapidly toward heavier nuclei. Among systems with established precision benchmarks, μd , $\mu^3\text{He}^+$, and $\mu^4\text{He}^+$ already stand out as the most promising near-term probes, with signal-to-precision ratios $\mathcal{R} \simeq 9.4$, 5.1, and 9.8, respectively. For future dedicated programs, the largest absolute Lamb-shift signal is predicted in $\mu^{31}\text{P}$, followed by several nuclei in the P-Si-Al-Mg region, indicating that medium-mass muonic atoms are a particularly favorable arena for short-range vector-force searches.

In the hyperfine sector, the survey reveals a clear and experimentally useful complementarity between mediator hypotheses. Because the protophobic vector benchmark is dominated by the neutron coupling, the vector scenario preferentially selects odd- N nuclei, with $\mu^{29}\text{Si}$ emerging as the leading $1S_{1/2}$ hyperfine target. By contrast, the pseudoscalar scenario is driven primarily by proton spin content and therefore favors odd- Z systems, with $\mu^{31}\text{P}$ yielding the largest predicted $1S_{1/2}$ hyperfine signal in the present survey. This odd- N versus odd- Z selectivity is one of the most important outcomes of the present work, because it shows that comparative spectroscopy across different nuclei can do more than test for the presence of a signal: it can help diagnose the coupling pattern and spin-parity structure of the underlying mediator.

The broader significance of the present study extends beyond the specific $X17$ interpretation of the ATOMKI anomalies. At a more general level, what we have constructed is a spectroscopy strategy for generic short-range Yukawa-type interactions in muonic atoms. Owing to the strong spatial compression of muonic wave functions, these systems are exceptionally sensitive to new forces with ranges of order a few to tens of femtometers, and the observable-dependent framework introduced here can be adapted straightforwardly to a wider class of vector, pseudoscalar, or other light-mediator scenarios. In this sense, the present work broadens the role of muonic-atom spectroscopy from a tool for testing selected anomaly-driven models to a more general precision platform for new-physics searches at the interface of atomic, nuclear, and particle physics.

The main theoretical limitation of the present survey lies in the Schmidt-model treatment of nuclear spin content in the hyperfine sector. While this level of description is sufficient for establishing the global hierarchy of targets, configuration mixing and core polarization can modify the effective spin fractions for individual nuclei, especially in the medium-mass region. Accordingly, the most important next theoretical step is to combine the present atomic framework with improved nuclear-structure calculations for the leading hyperfine candidates. On the experimental side, the results point to a natural two-stage program: near-term tests in μd and the helium sector, where precision benchmarks already exist, followed by longer-term dedicated studies of the most favorable heavier nuclei in the present survey, especially $\mu^{31}\text{P}$ and $\mu^{29}\text{Si}$.

Overall, the present survey shows that precision muonic-atom spectroscopy can provide not only competitive sensitivity to short-range fifth-force effects, but also genuine diagnostic power on their coupling structure. This makes muonic atoms a uniquely valuable laboratory for exploring light new interactions beyond the Standard Model.

ACKNOWLEDGMENTS

This work has been supported by the Research Program of State Key Laboratory of Heavy Ion Science and Technology, Institute of Modern Physics, Chinese Academy of Sciences (Grant No. HIST2025CS08), and the National Key R&D Program of China (Grant No. 2024YFE0109800 and 2024YFE0109802).

-
- [1] A. J. Krasznahorkay *et al.*, *Phys. Rev. Lett.* **116**, 042501 (2016), [arXiv:1504.01527](#).
 - [2] A. J. Krasznahorkay *et al.*, arXiv preprint (2019), anomalous e^+e^- pairs in ^4He transitions, [arXiv:1910.10459](#).
 - [3] J. L. Feng, B. Fornal, I. Galon, S. Gardner, J. Smolinsky, T. M. P. Tait, and P. Tanedo, *Phys. Rev. Lett.* **117**, 071803 (2016), [arXiv:1604.07411](#).
 - [4] U. Ellwanger and S. Moretti, *Journal of High Energy Physics* **2016**, 1 (2016).
 - [5] J. Kozaczuk, D. E. Morrissey, and S. Stroberg, *Physical Review D* **95**, 115024 (2017).
 - [6] A. Antognini, F. Nez, K. Schuhmann, F. D. Amaro, F. Biraben, J. M. Cardoso, D. S. Covita, A. Dax, S. Dhawan, M. Diepold, *et al.*, *Science* **339**, 417 (2013).
 - [7] K. Schuhmann, L. M. Fernandes, F. Nez, M. Abdou Ahmed, F. D. Amaro, P. Amaro, F. Biraben, T.-L. Chen, D. S. Covita, A. J. Dax, *et al.*, *Science* **388**, 854 (2025).
 - [8] U. D. Jentschura, *Phys. Rev. A* **101**, 062510 (2020), [arXiv:2003.07207](#).
 - [9] A. P. Martynenko, *Phys. At. Nucl.* **71**, 125 (2008).

- [10] A. A. Krutov and A. P. Martynenko, *Eur. Phys. J. D* **62**, 163 (2011).
- [11] E. Hiyama, Y. Kino, and M. Kamimura, *Progress in Particle and Nuclear Physics* **51**, 223 (2003).
- [12] M. Wang, W. J. Huang, F. G. Kondev, G. Audi, and S. Naimi, *Chin. Phys. C* **45**, 030003 (2021).
- [13] N. J. Stone, *Atomic Data and Nuclear Data Tables* **90**, 75 (2005).
- [14] I. Angeli and K. P. Marinova, *Atomic Data and Nuclear Data Tables* **99**, 69 (2013).
- [15] K. S. Krane, *Introductory Nuclear Physics* (Wiley, New York, 1987).
- [16] A. Bohr and B. R. Mottelson, *Nuclear Structure, Vols. I & II* (World Scientific, 1998) reprint edition.
- [17] E. A. Uehling, *Physical Review* **48**, 55 (1935).
- [18] U. D. Jentschura and V. A. Yerokhin, *Physical Review A* **73**, 062503 (2006).
- [19] M. Kamimura, *Physical Review A* **38**, 621 (1988).
- [20] Y. Suzuki and K. Varga, *Stochastic Variational Approach to Quantum-Mechanical Few-Body Problems*, Lecture Notes in Physics Monographs, Vol. 54 (Springer, Berlin, Heidelberg, 1998).
- [21] J. P. Leveille, *Nucl. Phys. B* **137**, 63 (1978).
- [22] M. Lindner, M. Platscher, and F. S. Queiroz, *Phys. Rept.* **731**, 1 (2018), arXiv:1610.06587.
- [23] M. g 2 Collaboration *et al.*, *Physical Review Letters* **135**, 101802 (2025).
- [24] R. Aliberti, T. Aoyama, E. Balzani, A. Bashir, G. Benton, J. Bijmens, V. Biloshytskyi, T. Blum, D. Boito, M. Bruno, *et al.*, arXiv preprint arXiv:2505.21476 (2025).
- [25] M. G. Mayer, *Physical Review* (1949).
- [26] J. H. D. Jensen, *Reviews of Modern Physics* (1955).
- [27] R. Neugart and G. Neyens, *Journal of Physics G: Nuclear and Particle Physics* (2017).
- [28] J. H. Kelley and T. collaborators, TUNL nuclear data evaluations (ensdf/tunl), <https://nucldata.tunl.duke.edu/>.
- [29] National Nuclear Data Center (NNDC), Nudat 3.0 database, <https://www.nndc.bnl.gov/nudat3/>.
- [30] Korea Atomic Energy Research Institute (KAERI), Chart of the nuclides, <https://atom.kaeri.re.kr/ton/>.
- [31] N. J. Stone, *Table of Nuclear Electric Quadrupole Moments*, Tech. Rep. INDC(NDS)-0650 (IAEA Nuclear Data Section, 2016).
- [32] S. Navas *et al.* (Particle Data Group), *Physical Review D* **110**, 030001 (2024).
- [33] L. W. Fullerton and G. Rinker Jr, *Physical Review A* **13**, 1283 (1976).
- [34] E. Borie and G. Rinker, *Reviews of Modern Physics* **54**, 67 (1982).
- [35] E. Borie, *Ann. Phys.* **327**, 733 (2012).
- [36] M. I. Eides, H. Grotch, and V. A. Shelyuto, *Theory of Light Hydrogenlike Atoms*, Springer Tracts in Modern Physics, Vol. 222 (2007).
- [37] R. N. Faustov and A. P. Martynenko, *J. Exp. Theor. Phys.* **98**, 39 (2004).
- [38] R. N. Faustov, A. P. Martynenko, G. A. Martynenko, and V. V. Sorokin, *Phys. Rev. A* **90**, 012520 (2014).
- [39] A. P. Martynenko, *J. Exp. Theor. Phys.* **106**, 690 (2008).
- [40] A. A. Krutov and A. P. Martynenko, *Phys. Rev. A* **84**, 052514 (2011).
- [41] J. J. Krauth, K. Schuhmann, M. A. Ahmed, F. D. Amaro, P. Amaro, F. Biraben, T.-L. Chen, D. S. Covita, A. J. Dax, M. Diepold, *et al.*, *Nature* **589**, 527 (2021).
- [42] R. Pohl, F. Nez, L. M. Fernandes, F. D. Amaro, F. Biraben, J. M. Cardoso, D. S. Covita, A. Dax, S. Dhawan, M. Diepold, *et al.*, *Science* **353**, 669 (2016).
- [43] J. Nuber, A. Adamczak, M. Abdou Ahmed, L. Affolter, F. Amaro, P. Amaro, A. Antognini, P. Carvalho, Y.-H. Chang, T.-L. Chen, *et al.*, *SciPost Physics Core* **6**, 057 (2022).
- [44] J. J. Krauth, M. Diepold, B. Franke, and others (CREMA Collaboration), *Science* **358**, 79 (2017).

Appendix A: Nuclear inputs and spin structure

1. Data sources and conventions

TABLE A1: Ground-state J^π , nuclear masses m_{nuc} [u], rms charge radii r_{ch} [fm; third column], and single-particle spin-sum projections (neutrons/protons) for stable nuclei with $Z \leq 15$. The r_{ch} values for ^1H , ^2H , and ^3He follow PDG/primary determinations [7, 44]; all other radii are taken from Angeli & Marinova [14]. For even–even nuclei with $I = 0$, the valence-orbital assignment is indicated as closed shell, while the spin-projection entries are marked by em dashes because no spin-dependent hyperfine contribution arises in the present framework.

Nuclide	m_{nuc} [u]	$\sqrt{\langle r^2 \rangle}$ (fm)	(Z, N)	Type	Ground J^π	Valence orbital	$\sum_i \mathbf{S}_n^i$	$\sum_i \mathbf{S}_p^i$
^1H	1.00727647	0.8409	(1,0)	Odd Z	$\frac{1}{2}^+$	p:1s _{1/2}	0	$+\frac{1}{2} \hbar \hat{\mathbf{J}}$
^2H	2.01355321	2.12799	(1,1)	Odd–Odd	1^+	p:1s _{1/2} ;n:1s _{1/2}	$+\frac{1}{2} \hbar \hat{\mathbf{J}}$	$+\frac{1}{2} \hbar \hat{\mathbf{J}}$
^3H	3.01550071	1.759	(1,2)	Odd Z	$\frac{1}{2}^+$	p:1s _{1/2}	0	$+\frac{1}{2} \hbar \hat{\mathbf{J}}$
^3He	3.01493224	1.97007	(2,1)	Odd N	$\frac{1}{2}^+$	n:1s _{1/2}	$+\frac{1}{2} \hbar \hat{\mathbf{J}}$	0
^4He	4.00150618	1.681	(2,2)	Even–Even	0^+	closed shell	—	—

⁶ Li	6.01347736	2.589	(3,3)	Odd–Odd	1 ⁺	p:1p _{3/2} ; n:1p _{3/2}	+ $\frac{1}{2} \hbar \hat{\mathbf{J}}$	+ $\frac{1}{2} \hbar \hat{\mathbf{J}}$
⁷ Li	7.01435791	2.444	(3,4)	Odd Z	$\frac{3}{2}^-$	p:1p _{3/2}	0	+ $\frac{1}{2} \hbar \hat{\mathbf{J}}$
⁹ Be	9.00998917	2.519	(4,5)	Odd N	$\frac{3}{2}^-$	n:1p _{3/2}	+ $\frac{1}{2} \hbar \hat{\mathbf{J}}$	0
¹⁰ B	10.01019478	2.427	(5,5)	Odd–Odd	3 ⁺	p:1p _{3/2} ; n:1p _{3/2}	+ $\frac{1}{2} \hbar \hat{\mathbf{J}}$	+ $\frac{1}{2} \hbar \hat{\mathbf{J}}$
¹¹ B	11.00656319	2.406	(5,6)	Odd Z	$\frac{3}{2}^-$	p:1p _{3/2}	0	+ $\frac{1}{2} \hbar \hat{\mathbf{J}}$
¹² C	11.99670964	2.470	(6,6)	Even–Even	0 ⁺	closed shell	—	—
¹³ C	13.00006448	2.461	(6,7)	Odd N	$\frac{1}{2}^-$	n:1p _{1/2}	− $\frac{1}{6} \hbar \hat{\mathbf{J}}$	0
¹⁴ N	13.99923557	2.558	(7,7)	Odd–Odd	1 ⁺	p:1p _{1/2} ; n:1p _{1/2}	− $\frac{1}{6} \hbar \hat{\mathbf{J}}$	− $\frac{1}{6} \hbar \hat{\mathbf{J}}$
¹⁵ N	14.99627046	2.612	(7,8)	Odd Z	$\frac{1}{2}^-$	p:1p _{1/2}	0	− $\frac{1}{6} \hbar \hat{\mathbf{J}}$
¹⁶ O	15.99052821	2.699	(8,8)	Even–Even	0 ⁺	closed shell	—	—
¹⁷ O	16.99474535	2.73	(8,9)	Odd N	$\frac{5}{2}^+$	n:1d _{5/2}	+ $\frac{1}{2} \hbar \hat{\mathbf{J}}$	0
¹⁸ O	17.99477321	2.775	(8,10)	Even–Even	0 ⁺	closed shell	—	—
²⁰ Ne	19.98695818	3.006	(10,10)	Even–Even	0 ⁺	closed shell	—	—
²¹ Ne	20.98836469	3.00	(10,11)	Odd N	$\frac{3}{2}^+$	n:1d _{3/2}	− $\frac{3}{10} \hbar \hat{\mathbf{J}}$	0
²⁴ Mg	23.97846462	3.057	(12,12)	Even–Even	0 ⁺	closed shell	—	—
²⁵ Mg	24.97925990	3.06	(12,13)	Odd N	$\frac{5}{2}^+$	n:1d _{5/2}	+ $\frac{1}{2} \hbar \hat{\mathbf{J}}$	0
²⁶ Mg	25.97601589	3.034	(12,14)	Even–Even	0 ⁺	closed shell	—	—
²⁷ Al	26.97441412	3.061	(13,14)	Odd Z	$\frac{5}{2}^+$	p:1d _{5/2}	0	+ $\frac{1}{2} \hbar \hat{\mathbf{J}}$
²⁸ Si	27.96925492	3.122	(14,14)	Even–Even	0 ⁺	closed shell	—	—
²⁹ Si	28.96882305	3.13	(14,15)	Odd N	$\frac{1}{2}^+$	n:2s _{1/2}	+ $\frac{1}{2} \hbar \hat{\mathbf{J}}$	0
³⁰ Si	29.96609852	3.134	(14,16)	Even–Even	0 ⁺	closed shell	—	—
³¹ P	30.96554333	3.190	(15,16)	Odd Z	$\frac{1}{2}^+$	p:2s _{1/2}	0	+ $\frac{1}{2} \hbar \hat{\mathbf{J}}$

2. Spin content and effective couplings

TABLE A2: Spin-content weights and nucleon couplings for *X17*. Columns list the nuclide, neutron/proton spin weights Δ_n, Δ_p , the spin-fraction-weighted effective couplings for the *hyperfine* sector $h_N^{(\text{eff})} = h_p' \Delta_p + h_n' \Delta_n$ (vector HFS) and $h_N^{(\text{eff})} = h_p \Delta_p + h_n \Delta_n$ (pseudoscalar HFS), the coherent coupling $Zh_p' + Nh_n'$ entering the *Lamb shift* via Eq. (6), and the experimental nuclear *g*-factor. For even-even nuclei with $I = 0$, hyperfine-related quantities are not applicable and are marked by ‘—’. The μ_{exp} values come from PDG (light nuclei) and Stone’s evaluated tables for stable nuclides.

Nuclide	Δ_n	Δ_p	$h_N^{(\text{eff})}$	$h_N^{(\text{eff})}$	$Zh_p' + Nh_n'$	$g_N^{(\text{exp})}$
¹ H	0	1	2.423×10^{-4}	-2.4×10^{-3}	2.423×10^{-4}	5.5856947
² H	$\frac{1}{4}$	$\frac{1}{4}$	8.176×10^{-4}	-4.725×10^{-4}	3.270×10^{-3}	1.7140255
³ H	0	1	2.423×10^{-4}	-2.4×10^{-3}	6.298×10^{-3}	17.836344
³ He	1	0	3.028×10^{-3}	5.1×10^{-4}	3.513×10^{-3}	−12.736573
⁴ He	—	—	—	—	6.541×10^{-3}	—
⁶ Li	$\frac{1}{4}$	$\frac{1}{4}$	8.176×10^{-4}	-4.725×10^{-4}	9.811×10^{-3}	4.907652
⁷ Li	0	$\frac{1}{3}$	8.075×10^{-5}	-8.0×10^{-4}	1.284×10^{-2}	15.117825
⁹ Be	$\frac{1}{3}$	0	1.009×10^{-3}	1.7×10^{-4}	1.611×10^{-2}	−7.021342
¹⁰ B	$\frac{1}{12}$	$\frac{1}{12}$	2.725×10^{-4}	-1.575×10^{-4}	1.635×10^{-2}	5.964865
¹¹ B	0	$\frac{1}{3}$	8.075×10^{-5}	-8.0×10^{-4}	1.938×10^{-2}	19.586006
¹² C	—	—	—	—	1.962×10^{-2}	—
¹³ C	− $\frac{1}{3}$	0	-1.009×10^{-3}	-1.7×10^{-4}	2.265×10^{-2}	18.130871
¹⁴ N	− $\frac{1}{12}$	− $\frac{1}{12}$	-2.725×10^{-4}	1.575×10^{-4}	2.290×10^{-2}	5.611513
¹⁵ N	0	− $\frac{1}{3}$	-8.075×10^{-5}	8.0×10^{-4}	2.592×10^{-2}	−8.432196
¹⁶ O	—	—	—	—	2.616×10^{-2}	—
¹⁷ O	$\frac{1}{5}$	0	6.056×10^{-4}	1.02×10^{-4}	2.919×10^{-2}	−12.780792
¹⁸ O	—	—	—	—	3.222×10^{-2}	—
²⁰ Ne	—	—	—	—	3.270×10^{-2}	—
²¹ Ne	− $\frac{1}{5}$	0	-6.056×10^{-4}	-1.02×10^{-4}	3.573×10^{-2}	−9.193117
²⁴ Mg	—	—	—	—	3.924×10^{-2}	—
²⁵ Mg	$\frac{1}{5}$	0	6.056×10^{-4}	1.02×10^{-4}	4.227×10^{-2}	−8.485658

²⁶ Mg	—	—	—	—	4.530×10^{-2}	—
²⁷ Al	0	$\frac{1}{5}$	4.846×10^{-5}	-4.8×10^{-4}	4.554×10^{-2}	39.020000
²⁸ Si	—	—	—	—	4.578×10^{-2}	—
²⁹ Si	1	0	3.028×10^{-3}	5.1×10^{-4}	4.881×10^{-2}	-31.928000
³⁰ Si	—	—	—	—	5.184×10^{-2}	—
³¹ P	0	1	2.423×10^{-4}	-2.4×10^{-3}	5.208×10^{-2}	69.605000

Appendix B: Vector- X_{17} -induced $2S_{1/2}$ - $2P_{1/2}$ Lamb shifts in muonic atoms

TABLE B1: Vector- X_{17} contribution to the $2S_{1/2}$ - $2P_{1/2}$ interval in muonic atoms, computed from the coherent potential $V_X = \frac{\hbar\mu}{4\pi}(Zh'_p + Nh'_n)\frac{e^{-m_X r}}{r}$ (Eq. (6)). Differences shown are $\Delta E_{X_{17}}^{(V)} = E_{X_{17}}^{(V)}(2S_{1/2}) - E_{X_{17}}^{(V)}(2P_{1/2})$ and $\Delta E_L^{(EM)} = E_L^{(EM)}(2S_{1/2}) - E_L^{(EM)}(2P_{1/2})$.

Nuclide	$E_{X_{17}}^{(V)}$ [meV]		$E_L^{(EM)}$ [eV]		$\Delta E_{X_{17}}^{(V)}$ [meV]	$\Delta E_L^{(EM)}$ [eV]	Ratio $\Delta E_{X_{17}}^{(V)}/\Delta E_L^{(EM)}$
	$2S_{1/2}$	$2P_{1/2}$	$2S_{1/2}$	$2P_{1/2}$			
¹ H	2.05125×10^{-3}	1.76275×10^{-6}	-2.21681×10^{-1}	-2.30039×10^{-2}	2.04949×10^{-3}	-1.98677×10^{-1}	-1.03157×10^{-5}
² H	3.20481×10^{-2}	3.05810×10^{-5}	-2.26034×10^{-1}	-2.71978×10^{-2}	3.20175×10^{-2}	-1.98837×10^{-1}	-1.61024×10^{-4}
³ H	6.49607×10^{-2}	6.42143×10^{-5}	-2.43984×10^{-1}	-2.88209×10^{-2}	6.48965×10^{-2}	-2.15163×10^{-1}	-3.01615×10^{-4}
³ He	2.45829×10^{-1}	9.72451×10^{-4}	-3.64950×10^0	-5.69311×10^{-1}	2.44856×10^{-1}	-3.08019×10^0	-7.94940×10^{-5}
⁴ He	4.69856×10^{-1}	1.88829×10^{-3}	-1.97317×10^0	-5.84337×10^{-1}	4.67968×10^{-1}	-1.38883×10^0	-3.36951×10^{-4}
⁶ Li	2.07425×10^0	1.91350×10^{-2}	-4.54573×10^0	-2.99490×10^0	2.05511×10^0	-1.55083×10^0	-1.32517×10^{-3}
⁷ Li	2.73512×10^0	2.53443×10^{-2}	-4.72410×10^0	-3.01603×10^0	2.70977×10^0	-1.70807×10^0	-1.58645×10^{-3}
⁹ Be	7.04029×10^0	1.16646×10^{-1}	-2.21206×10^1	-9.01208×10^0	6.92365×10^0	-1.31086×10^1	-5.28177×10^{-4}
¹⁰ B	1.21548×10^1	3.13017×10^{-1}	-2.15338×10^1	-2.04440×10^1	1.18417×10^1	-1.08981×10^0	-1.08658×10^{-2}
¹¹ B	1.44337×10^1	3.72639×10^{-1}	-1.48651×10^1	-2.04965×10^1	1.40610×10^1	5.63135×10^0	2.49692×10^{-3}
¹² C	2.20654×10^1	8.16132×10^{-1}	-3.22973×10^1	-3.95110×10^1	2.12493×10^1	7.21377×10^0	2.94566×10^{-3}
¹³ C	2.54461×10^1	9.44980×10^{-1}	-1.56057×10^2	-3.96263×10^1	2.45011×10^1	-1.16430×10^2	-2.10436×10^{-4}
¹⁴ N	3.60886×10^1	1.80258×10^0	-4.85038×10^2	-6.85058×10^1	3.42860×10^1	-4.16532×10^2	-8.23130×10^{-5}
¹⁵ N	4.08473×10^1	6.90205×10^{-1}	-4.96745×10^2	-2.04109×10^1	4.01571×10^1	-4.76334×10^2	-8.43044×10^{-5}
¹⁶ O	5.39722×10^1	3.52607×10^0	-1.97357×10^2	-1.11191×10^2	5.04461×10^1	-8.61668×10^1	-5.85448×10^{-4}
¹⁷ O	6.02308×10^1	3.94096×10^0	-2.19007×10^2	-1.11192×10^2	5.62898×10^1	-1.07815×10^2	-5.22094×10^{-4}
¹⁸ O	6.64632×10^1	4.35638×10^0	-2.48024×10^2	-1.11202×10^2	6.21069×10^1	-1.36822×10^2	-4.53925×10^{-4}
²⁰ Ne	1.04646×10^2	1.04895×10^1	-4.98728×10^3	-2.42051×10^2	9.41570×10^1	-4.74523×10^3	-1.98424×10^{-5}
²¹ Ne	1.14390×10^2	1.14731×10^1	-4.63871×10^3	-2.42193×10^2	1.02917×10^2	-4.39652×10^3	-2.34088×10^{-5}
²⁴ Mg	1.74876×10^2	2.47678×10^1	-7.29154×10^3	-4.62356×10^2	1.50109×10^2	-6.82919×10^3	-2.19805×10^{-5}
²⁵ Mg	1.88388×10^2	2.66985×10^1	-7.12773×10^3	-4.62545×10^2	1.61689×10^2	-6.66518×10^3	-2.42588×10^{-5}
²⁶ Mg	2.02208×10^2	2.86302×10^1	-6.50594×10^3	-4.62719×10^2	1.73578×10^2	-6.04322×10^3	-2.87227×10^{-5}
²⁷ Al	2.33870×10^2	3.83667×10^1	-1.73382×10^4	-6.32364×10^2	1.95503×10^2	-1.67058×10^4	-1.17027×10^{-5}
²⁸ Si	2.03453×10^2	2.89659×10^1	-7.67313×10^3	-4.63034×10^2	1.74487×10^2	-7.21009×10^3	-2.42004×10^{-5}
²⁹ Si	2.90383×10^2	5.33832×10^1	-8.84039×10^4	-8.07264×10^2	2.37000×10^2	-8.75966×10^4	-2.70558×10^{-6}
³⁰ Si	2.30301×10^2	3.28321×10^1	-7.57372×10^3	-4.63304×10^2	1.97469×10^2	-7.11042×10^3	-2.77718×10^{-5}
³¹ P	3.36263×10^2	7.22637×10^1	-3.74113×10^3	-1.20281×10^3	2.63999×10^2	-2.53832×10^3	-1.04005×10^{-4}

Appendix C: Vector- X_{17} -induced hyperfine structure in muonic atoms

1. $1S_{1/2}$ hyperfine structure

TABLE C1: Vector X_{17} in $1S_{1/2}$: level energies for non-even-even nuclei. Subcolumns are $F = S_N - J$ and $F = S_N + J$ (for $1S_{1/2}$, $J = \frac{1}{2}$). Differences shown are $\Delta E_{X_{17}}$ and ΔE_{EM} .

Nuclide	$E_{X_{17}}^{(V)}$ [meV]		$E_{HFS}^{(EM)}$ [eV]		$\Delta E_{X_{17}}^{(V)}$ [meV]	$\Delta E_{HFS}^{(EM)}$ [eV]	Ratio $\Delta E_{X_{17}}^{(V)}/\Delta E_{HFS}^{(EM)}$
	$F = S_N - J$	$F = S_N + J$	$F = S_N - J$	$F = S_N + J$			
¹ H	1.64795×10^{-2}	1.64538×10^{-2}	-1.37650×10^{-1}	4.55845×10^{-2}	-2.56779×10^{-5}	1.83235×10^{-1}	-1.40136×10^{-7}
² H	6.43445×10^{-2}	6.43132×10^{-2}	-3.29861×10^{-2}	1.66585×10^{-2}	-3.13625×10^{-5}	4.96446×10^{-2}	-6.31741×10^{-7}

³ H	2.00836×10^{-2}	2.00545×10^{-2}	-1.79037×10^{-1}	5.98639×10^{-2}	-2.91580×10^{-5}	2.38901×10^{-1}	-1.22051×10^{-7}
³ He	1.71420×10^0	1.71584×10^0	1.03392×10^0	-3.43674×10^{-1}	1.63759×10^{-3}	-1.37759×10^0	-1.18873×10^{-6}
⁶ Li	1.41133×10^0	1.41038×10^0	-8.91509×10^{-1}	4.44334×10^{-1}	-9.51181×10^{-4}	1.33584×10^0	-7.12046×10^{-7}
⁷ Li	1.40571×10^0	1.40308×10^0	-2.99664×10^0	1.76060×10^0	-2.62341×10^{-3}	4.75724×10^0	-5.51411×10^{-7}
⁹ Be	3.64731×10^0	3.64770×10^0	2.88950×10^0	-1.71041×10^0	3.84843×10^{-4}	-4.59991×10^0	-8.36672×10^{-8}
¹⁰ B	1.70084×10^0	1.69689×10^0	-9.20307×10^0	6.92823×10^0	-3.94983×10^{-3}	1.61313×10^1	-2.44823×10^{-7}
¹¹ B	5.05247×10^{-1}	5.04533×10^{-1}	-1.67214×10^1	1.08051×10^1	-7.13596×10^{-4}	2.75264×10^1	-2.59215×10^{-8}
¹³ C	-9.61119×10^0	-9.60465×10^0	-9.51785×10^0	3.22829×10^0	6.53708×10^{-3}	1.27461×10^1	5.12922×10^{-7}
¹⁴ N	-3.65623×10^0	-3.65430×10^0	-5.37053×10^0	2.70519×10^0	1.93417×10^{-3}	8.07572×10^0	2.39494×10^{-7}
¹⁵ N	-1.08190×10^0	-1.08308×10^0	5.03209×10^0	-1.90055×10^0	-1.17717×10^{-3}	-6.93264×10^0	1.69774×10^{-7}
¹⁷ O	1.10691×10^1	1.10975×10^1	1.05051×10^2	-7.49520×10^1	2.83746×10^{-2}	-1.79903×10^2	-1.57696×10^{-7}
²¹ Ne	-1.69286×10^1	-1.69378×10^1	1.86558×10^1	-1.02988×10^1	-9.16707×10^{-3}	-2.89545×10^1	3.16603×10^{-7}
²⁵ Mg	2.38868×10^1	2.38581×10^1	4.25753×10^1	-3.55384×10^1	-2.87315×10^{-2}	-7.81136×10^1	3.67827×10^{-7}
²⁷ Al	2.22602×10^0	2.25491×10^0	-1.47751×10^2	7.62922×10^2	2.88963×10^{-2}	9.10674×10^2	3.17235×10^{-8}
²⁹ Si	1.57020×10^2	1.56377×10^2	7.44958×10^1	-3.22391×10^1	-6.43146×10^{-1}	-1.06735×10^2	6.02570×10^{-6}
³¹ P	1.37586×10^1	1.38510×10^1	-6.07764×10^2	1.29332×10^2	9.23910×10^{-2}	7.37096×10^2	1.25331×10^{-7}

2. $2P_{1/2}$ hyperfine structure

TABLE C2: Vector X_{17} in $2P_{1/2}$: level energies for non-even-even nuclei.

Nuclide	$E_{X_{17}}^{(V)}$ [meV]		$E_{\text{HFS}}^{(\text{EM})}$ [eV]		$\Delta E_{X_{17}}^{(V)}$ [meV]	$\Delta E_{\text{HFS}}^{(\text{EM})}$ [eV]	Ratio $\Delta E_{X_{17}}^{(V)}/\Delta E_{\text{HFS}}^{(\text{EM})}$
	$F = S_N - J$	$F = S_N + J$	$F = S_N - J$	$F = S_N + J$			
¹ H	1.76523×10^{-6}	1.76193×10^{-6}	-1.40533×10^{-3}	4.68424×10^{-4}	-3.30573×10^{-9}	1.87376×10^{-3}	-1.76422×10^{-9}
² H	7.65256×10^{-6}	7.64300×10^{-6}	-3.47656×10^{-4}	1.73826×10^{-4}	-9.55542×10^{-9}	5.21482×10^{-4}	-1.83229×10^{-8}
³ H	2.47196×10^{-6}	2.47000×10^{-6}	-1.93300×10^{-3}	6.44301×10^{-4}	-1.96472×10^{-9}	2.57730×10^{-3}	-7.62442×10^{-10}
³ He	8.38409×10^{-4}	8.38129×10^{-4}	1.39667×10^{-2}	-4.65586×10^{-3}	-2.79382×10^{-7}	-1.86226×10^{-2}	1.50034×10^{-8}
⁶ Li	1.59510×10^{-3}	1.59430×10^{-3}	-1.31292×10^{-2}	6.56444×10^{-3}	-7.99141×10^{-7}	1.96936×10^{-2}	-4.05871×10^{-8}
⁷ Li	1.59460×10^{-3}	1.59342×10^{-3}	-4.36932×10^{-2}	2.62136×10^{-2}	-1.18290×10^{-6}	6.99068×10^{-2}	-1.69200×10^{-8}
⁹ Be	7.30729×10^{-3}	7.30507×10^{-3}	3.79765×10^{-2}	-2.27869×10^{-2}	-2.21743×10^{-6}	-6.07634×10^{-2}	3.64978×10^{-8}
¹⁰ B	5.21933×10^{-3}	5.21513×10^{-3}	-9.12873×10^{-2}	6.84604×10^{-2}	-4.19645×10^{-6}	1.59748×10^{-1}	-2.62663×10^{-8}
¹¹ B	1.55321×10^{-3}	1.55230×10^{-3}	-1.70912×10^{-1}	1.02534×10^{-1}	-9.09914×10^{-7}	2.73446×10^{-1}	-3.32723×10^{-9}
¹³ C	-4.21071×10^{-2}	-4.20964×10^{-2}	-1.39917×10^{-1}	4.66361×10^{-2}	1.06944×10^{-5}	1.86553×10^{-1}	5.73169×10^{-8}
¹⁴ N	-2.14525×10^{-2}	-2.14468×10^{-2}	-8.54219×10^{-2}	4.27106×10^{-2}	5.69459×10^{-6}	1.28133×10^{-1}	4.44482×10^{-8}
¹⁵ N	-6.37011×10^{-3}	-6.36952×10^{-3}	9.00132×10^{-2}	-3.00064×10^{-2}	5.85995×10^{-10}	-1.20020×10^{-1}	-4.88209×10^{-12}
¹⁷ O	8.17780×10^{-2}	8.17614×10^{-2}	4.21766×10^{-1}	-3.01299×10^{-1}	-1.65817×10^{-5}	-7.23065×10^{-1}	2.29327×10^{-8}
²¹ Ne	-1.94430×10^{-1}	-1.94391×10^{-1}	3.45176×10^{-1}	-2.06942×10^{-1}	3.89972×10^{-5}	-5.52118×10^{-1}	-7.06301×10^{-8}
²⁵ Mg	3.82583×10^{-1}	3.82507×10^{-1}	6.57331×10^{-1}	-4.69650×10^{-1}	-7.64737×10^{-5}	-1.12698×10^0	6.78643×10^{-8}
²⁷ Al	4.08235×10^{-2}	4.07973×10^{-2}	-3.56816×10^0	2.55029×10^0	-2.61560×10^{-5}	6.11845×10^0	-4.27545×10^{-9}
²⁹ Si	3.31316×10^0	3.31403×10^0	1.47523×10^0	-4.93339×10^{-1}	8.70304×10^{-4}	-1.96857×10^0	-4.42102×10^{-7}
³¹ P	3.36530×10^{-1}	3.36420×10^{-1}	-3.69986×10^0	1.23304×10^0	-1.09336×10^{-4}	4.93291×10^0	-2.21644×10^{-8}

Appendix D: Pseudoscalar- X_{17} -induced hyperfine structure in muonic atoms

1. $1S_{1/2}$ hyperfine structure

TABLE D1: Pseudoscalar X_{17} : level energies for non-even-even nuclei. Subcolumns are $F = S_N - J$ and $F = S_N + J$ (for $1S_{1/2}$, $J = \frac{1}{2}$).

Nuclide	$E_{X_{17}}^{(A)}$ [meV]		$E_{\text{HFS}}^{(\text{EM})}$ [eV]		$\Delta E_{X_{17}}$ [meV]	ΔE_{EM} [eV]	Ratio
	$F = S_N - J$	$F = S_N + J$	$F = S_N - J$	$F = S_N + J$			
¹ H	-1.62898×10^{-4}	5.23107×10^{-5}	-1.37796×10^{-1}	4.56325×10^{-2}	2.15208×10^{-4}	1.83428×10^{-1}	1.17326×10^{-6}
² H	-1.92273×10^{-5}	1.04034×10^{-5}	-3.15703×10^{-2}	1.59376×10^{-2}	2.96307×10^{-5}	4.75079×10^{-2}	6.23710×10^{-7}
³ H	-6.48738×10^{-5}	2.22504×10^{-5}	-1.78672×10^{-1}	5.97417×10^{-2}	8.71242×10^{-5}	2.38414×10^{-1}	3.65452×10^{-7}
³ He	2.08131×10^{-4}	-6.84764×10^{-5}	1.02733×10^0	-3.41520×10^{-1}	-2.76607×10^{-4}	-1.36885×10^0	2.02053×10^{-7}

⁶ Li	-5.46531×10^{-4}	2.70768×10^{-4}	-8.91760×10^{-1}	4.44348×10^{-1}	8.17298×10^{-4}	1.33611×10^0	6.11567×10^{-7}
⁷ Li	-8.03830×10^{-4}	4.02161×10^{-4}	-2.75675×10^0	1.56991×10^0	1.20699×10^{-3}	4.32666×10^0	2.78923×10^{-7}
⁹ Be	5.56011×10^{-4}	-3.33877×10^{-4}	2.69550×10^0	-1.61844×10^0	-8.89888×10^{-4}	-4.31393×10^0	2.06329×10^{-7}
¹⁰ B	1.28740×10^{-2}	-3.49457×10^{-3}	-1.84258×10^1	6.45649×10^0	-1.63685×10^{-2}	2.48823×10^1	6.57740×10^{-7}
¹¹ B	-8.87346×10^{-3}	5.07868×10^{-3}	-1.75574×10^1	1.02008×10^1	1.39521×10^{-2}	2.77582×10^1	5.02488×10^{-7}
¹³ C	-9.66528×10^{-4}	3.25034×10^{-4}	-9.72284×10^0	3.25666×10^0	1.29156×10^{-3}	1.29795×10^1	9.95052×10^{-8}
¹⁴ N	7.86014×10^{-4}	-7.46216×10^{-4}	-3.74528×10^0	2.55625×10^0	-1.53223×10^{-3}	6.30153×10^0	2.43208×10^{-7}
¹⁵ N	-5.27350×10^{-3}	1.40266×10^{-3}	5.35887×10^0	-1.58260×10^0	6.67616×10^{-3}	-6.94147×10^0	9.61906×10^{-7}
¹⁷ O	6.76740×10^{-4}	-3.56875×10^{-3}	1.43279×10^1	-3.12414×10^1	-4.24549×10^{-3}	-4.55692×10^1	9.31548×10^{-8}
²¹ Ne	-5.18206×10^{-3}	2.89136×10^{-3}	1.90020×10^1	-1.03316×10^1	8.07342×10^{-3}	-2.93336×10^1	2.75187×10^{-7}
²⁵ Mg	4.43419×10^{-3}	-7.05199×10^{-3}	-2.97668×10^1	-3.87654×10^1	-1.14862×10^{-2}	-6.85322×10^1	1.67594×10^{-7}
²⁷ Al	-2.85227×10^{-2}	2.45572×10^{-2}	-1.73896×10^2	1.42511×10^2	5.30799×10^{-2}	3.16407×10^2	1.67780×10^{-7}
²⁹ Si	2.36601×10^{-2}	-1.02860×10^{-2}	9.80510×10^1	-4.08207×10^1	-3.39461×10^{-2}	-1.38872×10^2	2.44485×10^{-7}
³¹ P	-7.07436×10^{-1}	2.17207×10^{-3}	-1.15398×10^3	2.16058×10^0	7.09608×10^{-1}	1.15614×10^3	6.13708×10^{-7}

2. $2P_{1/2}$ hyperfine structure

TABLE D2: Pseudoscalar $X17$ in $2P_{1/2}$: level energies for non-even-even nuclei. Subcolumns are $F = S_N - J$ and $F = S_N + J$ (for $2P_{1/2}$, $J = \frac{1}{2}$). Differences shown are ΔE_{X17} and ΔE_{EM} .

Nuclide	$E_{X17}^{(A)}$ [μeV]		$E_{\text{HFS}}^{(\text{EM})}$ [eV]		ΔE_{X17} [μeV]	$\Delta E_{\text{HFS}}^{(\text{EM})}$ [eV]	Ratio $\Delta E_{X17}^{(A)}/\Delta E_{\text{HFS}}^{(\text{EM})}$
	$F = S_N - J$	$F = S_N + J$	$F = S_N - J$	$F = S_N + J$			
¹ H	-7.20457×10^{-6}	2.40640×10^{-6}	-1.40533×10^{-3}	4.68424×10^{-4}	9.61097×10^{-6}	1.87376×10^{-3}	5.12925×10^{-9}
² H	-4.67867×10^{-3}	-4.67258×10^{-3}	-3.51268×10^{-4}	1.75632×10^{-4}	6.09541×10^{-6}	5.26900×10^{-4}	1.15679×10^{-8}
³ H	-3.24857×10^{-6}	1.08512×10^{-6}	-1.93300×10^{-3}	6.44301×10^{-4}	4.33369×10^{-6}	2.57730×10^{-3}	1.68159×10^{-9}
³ He	7.56931×10^{-6}	-2.51092×10^{-6}	1.39667×10^{-2}	-4.65586×10^{-3}	-1.00802×10^{-5}	-1.86226×10^{-2}	5.41320×10^{-10}
⁶ Li	1.61007×10^{-5}	-8.05892×10^{-6}	-1.31292×10^{-2}	6.56443×10^{-3}	-2.41596×10^{-5}	1.96936×10^{-2}	1.22676×10^{-9}
⁷ Li	3.35391×10^{-5}	-2.00607×10^{-5}	-4.36932×10^{-2}	2.62136×10^{-2}	-5.35998×10^{-5}	6.99068×10^{-2}	7.66794×10^{-10}
⁹ Be	-8.22068×10^{-5}	4.93810×10^{-5}	3.79765×10^{-2}	-2.27869×10^{-2}	1.31588×10^{-4}	-6.07634×10^{-2}	-2.16578×10^{-9}
¹⁰ B	-8.69145×10^{-4}	6.51198×10^{-4}	-9.12873×10^{-2}	6.84604×10^{-2}	1.52034×10^{-3}	1.59748×10^{-1}	9.51807×10^{-9}
¹¹ B	1.46153×10^{-3}	-8.75433×10^{-4}	-1.70912×10^{-1}	1.02534×10^{-1}	-2.33697×10^{-3}	2.73446×10^{-1}	8.54500×10^{-9}
¹³ C	5.03453×10^{-4}	-1.67676×10^{-4}	-1.39918×10^{-1}	4.66361×10^{-2}	-6.71129×10^{-4}	1.86554×10^{-1}	-3.59774×10^{-9}
¹⁴ N	-1.36603×10^{-3}	6.81908×10^{-4}	-8.54247×10^{-2}	4.27093×10^{-2}	2.04794×10^{-3}	1.28134×10^{-1}	1.59790×10^{-8}
¹⁵ N	1.81513×10^{-3}	-6.04287×10^{-4}	2.66533×10^{-2}	-8.88422×10^{-3}	-2.41942×10^{-3}	-3.55375×10^{-2}	6.80751×10^{-8}
¹⁷ O	-2.76768×10^{-3}	1.97815×10^{-3}	4.21767×10^{-1}	-3.01300×10^{-1}	4.74582×10^{-3}	-7.23067×10^{-1}	-6.56434×10^{-9}
²¹ Ne	5.12853×10^{-3}	-3.11381×10^{-3}	3.45073×10^{-1}	-2.07226×10^{-1}	-8.24233×10^{-3}	-5.52298×10^{-1}	1.49225×10^{-8}
²⁵ Mg	-1.65151×10^{-2}	1.17959×10^{-2}	6.57311×10^{-1}	-4.69533×10^{-1}	2.83109×10^{-2}	-1.12684×10^0	-2.51234×10^{-8}
²⁷ Al	1.05364×10^{-1}	-7.52779×10^{-2}	-3.56918×10^0	2.54884×10^0	-1.80642×10^{-1}	6.11802×10^0	-2.95252×10^{-8}
²⁹ Si	-6.88009×10^{-2}	2.26938×10^{-2}	1.47701×10^0	-4.91593×10^{-1}	9.14947×10^{-2}	-1.96861×10^0	-4.64815×10^{-8}
³¹ P	4.04528×10^{-1}	-1.34221×10^{-1}	-3.70087×10^0	1.23251×10^0	-5.38749×10^{-1}	4.93338×10^0	-1.09198×10^{-7}